Investigation of Fluid Flow and Steel Cleanliness in the Continuous Casting Strand

LIFENG ZHANG, SUBO YANG, KAIKE CAI, JIYING LI, XIAOGUANG WAN, and BRIAN G. THOMAS

Fluid flow in the mold region of the continuous slab caster at Panzhihua Steel is investigated with 0.6-scale water model experiments, industrial measurements, and numerical simulations. In the water model, multiphase fluid flow in the submerged entry nozzle (SEN) and the mold with gas injection is investigated. Top surface level fluctuations, pressure at the jet impingement point, and the flow pattern in the mold are measured with changing submergence depth, SEN geometry, mold width, water flow rate, and argon gas flow rate. In the industrial investigation, the top surface shape and slag thickness are measured, and steel cleanliness including inclusions and the total oxygen (TO) content are quantified and analyzed, comparing the old and new nozzle designs. Three kinds of fluid flow pattern are observed in the SEN: "bubbly flow," "annular flow," and an intermediate critical flow structure. The annular flow structure induces detrimental asymmetrical flow and worse level fluctuations in the mold. The SEN flow structure depends on the liquid flow rate, the gas flow rate, and the liquid height in the tundish. The gas flow rate should be decreased at low casting speed in order to maintain stable bubbly flow, which produces desirable symmetrical flow. Two main flow patterns are observed in the mold: single roll and double roll. The single-roll flow pattern is generated by large gas injection, small SEN submergence depth, and low casting speed. To maintain a stable double-roll flow pattern, which is often optimal, the argon should be kept safely below a critical level. The chosen optimal nozzle had 45-mm inner bore diameter, downward 15 deg port angle, 2.27 port-to-bore area ratio, and a recessed bottom. The pointed-bottom SEN generates smaller level fluctuations at the meniscus, larger impingement pressure, deeper impingement, and more inclusion entrapment in the strand than the recess-bottom SEN. Mass balances of inclusions in the steel slag from slag and slab measurements show that around 20 pct of the alumina inclusions are removed from the steel into the mold slag. However, entrainment of the mold slag itself is a critical problem. Inclusions in the steel slabs increase twofold during ladle changes and tenfold during the start and end of a sequence. All of the findings in the current study are important for controlling slag entrainment.

DOI: 10.1007/s11663-006-9007-0

I. INTRODUCTION

FLUID flow in the submerged entry nozzle (SEN) and the continuous casting mold is important due to its effect on many phenomena related to steel quality, such as the transport of argon bubbles and inclusions, transient waves and fluctuations of the top surface, the transport of superheat, meniscus freezing, shell thinning from the jet impinging upon the solidifying shell, thermal stress, and crack formation. The entrainment of mold slag due to excessive surface velocities and level fluctuations is one of the most important causes of defects found in steel products.[1–9]

The main flow-related phenomena that cause slag entrainment and surface quality problems are shown in Figure 1.[10] If the jet from the SEN outport strongly impinges on the narrow face and splits to flows upward along the narrow face, it will lift the level of the molten steel, changing its profile and also generating large level fluctuations near the meniscus. This also pushes slag away from the narrow face, leading to surface quality problems.[10–17] Direct jet impingement of the jet onto the steel-slag interface associated with a single-roll flow pattern, such as induced by excessive gas bubble injection,[18] is even more detrimental. Excessive velocity of the molten steel across the top surface may shear off fingers of slag into the steel.[19–27] Turbulence and level fluctuations at the top surface can induce slag entrainment at the meniscus and surface defects. Flow problems, such as uneven flow discharge from opposite ports of the SEN,[10] may cause asymmetric and

LIFENG ZHANG, Professor, is with the Department of Materials Science and Engineering, Norwegian University of Science and Technology (NTNU), 7491 Trondheim, Norway. Contact e-mail: lifeng.zhang@material.ntnu.no. SUBO YANG, Chief Researcher, is with the Technical Research Center, Panzhihua Iron and Steel Company, Panzhihua 617023, Sichuan Province, People's Republic of China. KAIKE CAI, Professor, and JIYING LI and XIAOGUANG WAN, Graduate students, are with the School of Metallurgy, University of Science and Technology Beijing, Beijing 100083, People's Republic of China. BRIAN G. THOMAS, Professor, is with the Department of Mechanical and Industrial Engineering, University of Illinois at Urbana–Champaign, Urbana, IL 61801, USA.
Manuscript submitted June 14, 2005.

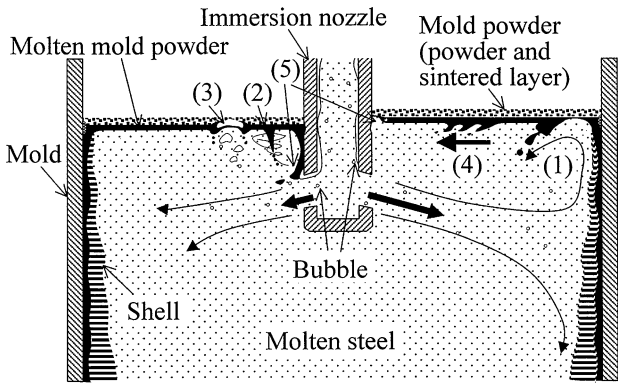

Fig. 1—Mechanisms of slag entrainment in the continuous casting mold.[10]

unsteady flow in the mold[28] or periodic oscillations of the level. High speed surface flows or asymmetrical flow in the mold may also induce vortices near the SEN.[10,29] These are other important causes of slag entrainment. Emulsification of the slag/steel interface, such as caused by the rupture of bubbles floating to this interface,[16,30] is also dangerous. The slag foam is easily entrained into the steel flow. Alternatively, slag may be sucked down along the SEN wall due to flow recirculation and the low pressure region just above the SEN port exits.[10] Mold slag may enter the upper portion of the ports and cause clogging problems, or become entrained into the jet and cause serious slag entrainment problems. Thus, the fluid flow pattern in the mold and level fluctuations are of great importance to slag entrainment quality problems,[21] and large level fluctuations correlate with more surface defects in the steel product.[22]

In the current article, fluid flow in the SEN and the mold of the slab continuous caster at Panzhihua Steel is investigated using water models, numerical simulations, and industrial measurements. First, the water model is used to investigate the fluid flow pattern in the SEN, which is one of the sources of asymmetrical flow in the mold. Then, flow in the mold is quantified by measuring the magnitude of the top surface level fluctuations, the pressure near the jet impingement point on the narrow face, and the flow pattern shape for different SEN geometry, submergence depth, mold width, water flow rate, and gas flow rate. The single-roll and double-roll flow pattern and the top surface emulsification induced by bubbles are noted. In the mathematical simulation, three-dimensional fluid flow and particle transport are calculated in the water model of the tundish, the SEN, and the mold. In the industrial trial, the thickness of the liquid slag layer, and the inclusion content in the steel and slag are measured, to determine the extent of inclusion removal in the mold, relative to inclusions entrapped in the steel product. The effect of the SEN well shape on steel cleanliness is also investigated. Finally, improved design and operating conditions are chosen to improve fluid flow and steel cleanliness in the plant.

II. INVESTIGATION METHODS

A. *Similarity Criterion of Water Model Experiments*

Extensive past work has employed physical water models to investigate fluid flow phenomena in the mold region of the continuous casting process.[19,31–46] The first study was carried out by Afanaseva *et al.*[31] for a straight bore nozzle system. Heaslip *et al.* extensively studied the fluid flow in SENs under stopper-rod control and slide-gate control.[35,36] Gupta investigated the residence time distribution,[37] asymmetry and oscillation of the fluid flow pattern,[38,39] and slag entrainment.[40,41] Tanaka *et al.*[42] and Wang *et al.*[44] studied the influence of wettability on the behavior of argon bubbles and fluid flow. Teshima *et al.*[19] and Iguchi *et al.*[43] studied slag entrainment. However, there are few articles with measurements of level fluctuations at the meniscus.[19,47] Only a few articles investigate impingement pressure on the narrow face and believe that lower pressure is better.[48,49]

In the current work, the Weber–Froude similarity criterion was used to design the water model for the gas-water two-phase fluid flow phenomena of interest. For the high-velocity flow conditions present in a steel continuous caster, fully developed turbulent flow conditions are always produced, so achieving Reynold's similarity by matching the ratio of the momentum and diffusion forces was judged to be less important, as long as fully turbulent flow conditions are maintained.

First, invoking the Froude similarity to ensure equal ratios of the momentum and buoyancy forces in the water model (w) and steel caster (s) gives

$$\mathrm{Fr} = \left(\frac{U^2}{gL}\right)_w = \left(\frac{U^2}{gL}\right)_s \qquad [1]$$

where Fr is the Froude number, U is a characteristic velocity (m/s), g is the gravitational acceleration rate (m/s^2), L is a characteristic length (m). Substituting the geometry scale factor, $\lambda = L_w/L_s$, into Eq. [1] gives

$$\frac{U_w}{U_s} = \sqrt{\lambda} \qquad [2]$$

Second, applying Weber similarity to match the ratio of the momentum and surface tension forces implies

$$\mathrm{We} = \left(\frac{\rho U^2 L}{\sigma}\right)_w = \left(\frac{\rho U^2 L}{\sigma}\right)_s \qquad [3]$$

where We is the Weber number; ρ is the liquid density, 7020 kg/m^3 for molten steel and 998 kg/m^3 for water; and σ is the surface tension, 1.6 for molten steel and 0.073 N/m for water.

Combining Eqs. [2] and [3] gives

$$\lambda = \left(\frac{\rho_S}{\rho_w}\frac{\sigma_w}{\sigma_S}\right)^{1/2} \sim 0.6 \qquad [4]$$

Thus, a 0.6-scale water model can satisfy both Froude similarity and Weber similarity simultaneously. An

additional requirement is to scale down the water flow rate (Q_w) relative to the molten steel throughput (Q_S) (m^3/h) according to

$$\frac{Q_w}{Q_s} = \frac{U_w L_w^2}{U_s L_s^2} = \lambda^{2.5} = 0.279 \quad [5]$$

The casting speed (measured for the solid strand) is related to the liquid steel flow rate from the following mass balance, which considers the effect of steel solidification on the density.

$$V_C = \frac{Q_S}{S}\left(\frac{1\text{ h}}{60\text{ min}}\right)\left(\frac{7020}{7800}\right) \quad [6]$$

where V_C is the steel casting speed (m/min), Q_S is the liquid steel flow rate (m^3/h), S is the cross-sectional area of the strand (m^2), and 7800/7020 is the ratio of solid to liquid steel densities. Combining Eqs. [5] and [6] gives the relationship between casting speed in the real caster and flow rate in the water model (Table I). For a 200 mm × 900 mm strand,

$$V_C\ (\text{m/min}) = 0.298\ Q_w(\text{m}^3/\text{h}) \quad [7]$$

and for a 200 mm × 1250 mm strand,

$$V_C = 0.214\ Q_w \quad [8]$$

A suggested argon flow rate to use in the steel continuous casting is found by matching the modified Froude numbers in the water model and steel caster,

$$\text{Fr}' = \frac{\rho_{N_2} V_{N_2}^2}{(\rho_w - \rho_{N_2}) \cdot g \cdot L_w} = \frac{\rho_{Ar} V_{Ar}^2}{(\rho_S - \rho_{Ar}) \cdot g \cdot L_S} \quad [9]$$

where Fr′ is the modified Froude number, ρ_g and ρ_l are the density of the gas and liquid (kg/m^3), and V_g is the gas velocity (m/s). Here, ρ_w = 998 kg/m^3, ρ_s = 7020 kg/m^3, ρ_{Ar} = 1.783 kg/m^3, and ρ_{N_2} = 1.251 kg/m^3. The gas flow rate is $Q_g = V_g \cdot 1/4\pi D_n^2$, where D_n is the diameter of the hole in the bottom of the stopper rod through which the gas enters the SEN. In the water model, $D_{n,w}$ = 0.004 m, and in the steel caster, $D_{n,s}$ = 0.005 m.

Evaluating Eq. [9] at standard pressure (1 atm) and 1550 °C gives

$$Q_{Ar} = 4.481 Q_{N2} \quad [10]$$

Considering the sixfold increase in volume during heating of the injected gas to steel temperature, the argon gas flow at the standard temperature (0 °C) should be

$$Q_{Ar} = 0.671 Q_{N2} \quad [11]$$

It should be mentioned that although the Froude, Weber, and modified-Froude similarity criteria are all simultaneously satisfied, the similarity between the water model and steel caster needs further investigation. Recent work has found that the multiphase fluid flow pattern in a 0.4-scale water model based on Froude similarity did not match the fluid flow pattern in the molten steel caster, although a numerical simulation was found to match both.[50,51]

B. *Orthogonal Design of Water Model Experiments*

A schematic of the water model is shown in Figure 2. A straight-mold steel caster of a 200-mm-thick and 1250-mm-wide strand is modeled with a water model that is 1200 mm in length, 120 mm in thickness, and varies in width from 774.6 mm at the top to 753.3 mm at the bottom. A second strand width of 900 mm is modeled with a top width of 557.7 mm and bottom width of 542.4 mm. The example SEN configuration is also shown in Figure 2. The N_2 gas, used to model the argon gas in the molten steel, is injected into the mold through a central circular hole (4 mm in diameter) in the bottom of the stopper rod.

First, the flow rate and water heights in the tundish and mold are maintained steady for 5 minutes by adjusting the position of the stopper rod and the outlet flow valve. The water height in the tundish is 600 mm if not specified otherwise. Then, the level fluctuation, impingement pressure, and location of the lower roll center are each measured three times, and the means are recorded. The definition of the level fluctuation is the mean of the five largest level fluctuations during each 40-second measurement. This is because large level fluctuations account more for the slag entrainment than small ones. The impingement pressure is the mean of the measured pressure for 40 seconds measured near the impingement point of the narrow face, subtracting the static water pressure ($\rho_w gh$). The location of the center of the lower roll is measured from the top surface.

All initial flow pattern studies were conducted with the recessed nozzle. The effects of six factors of casting speed, SEN submergence depth (the distance from the meniscus to the top of SEN outports), gas flow rate, SEN outport angle, inner diameter of SEN, area ratio ψ (the total area of the two outports to the SEN bore cross-sectional area), and bottom well shape on the level fluctuation, impingement pressure, and location of the

Table I. Relationship between the Flow Rate and the Casting Speed

	casting speed (m/min)	0.8	1.0	1.2	1.4	1.6	1.8
200 mm × 900 mm slab	steel throughput (m^3/h)	9.60	11.90	14.28	16.66	19.04	21.41
	water throughput (m^3/h)	2.68	3.32	3.98	4.65	5.31	5.98
200 mm × 1250 mm slab	steel throughput (m^3/h)	13.22	16.52	19.83	23.14	26.44	30.00
	water throughput (m^3/h)	3.69	4.61	5.53	6.46	7.38	8.37

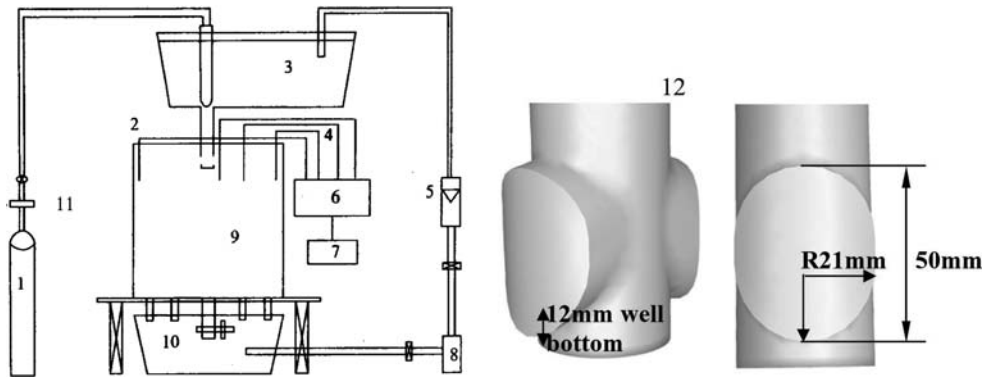

Fig. 2—Schematic of the water model experiment (1: N_2 tank, 2: pressure measurement probe, 3: tundish, 4: level fluctuation measurement probes, 5: water flow meter, 6: data collection system, 7: computer, 8: pump, 9: mold, 10: water collection tank, 11: gas flow meter, and 12: dimension of the SEN outports).

lower roll center are investigated. For each factor, there are five values to be investigated, as shown in Table II. Each single water model experiment combines one set values of factors. In general, if there are k factors with n values, the total number of combinations is n^k. For the current study, the total number of combinations is $5^6 = 15{,}625$. When the number of factors and the number of values are small, it may be feasible to test all the combinations. Very often, it is not possible or cost effective to test all the combinations. It is desirable to sample a small but representative sample of combinations for testing. The orthogonal experimental design (OED) was developed for this purpose.[52–57] It provides a series of orthogonal arrays for different numbers of factors and different numbers of values. The term $L_m(n^k)$ denotes an orthogonal array for k factors and n values, where L denotes a Latin square and m is the number of combinations to be tested. An example of $L_9(3^4)$ is shown in Table III. In this table, each row represents a combination of factor values. The orthogonality of an array means that (1) for the factor in any column, every value occurs the same number of times; (2) for two factors in any two columns, every combination of two values occurs the same number of times; and (3) the selected combinations are uniformly distributed over the entire space of all the possible combinations. It has been proved that the orthogonal design is optimal to use a far reduced number of selected combinations to well represent all the possible combinations.[52,57] The OED method has been used for the water model experiments of the fluid flow in continuous casting mold.[58,59] For the current studies, measurements in the water model with recess-bottom SEN were performed for 25 different sets of conditions for each of the two size water models according to the three rules of OED, and examples are given in Table IV.

Table II. Parameters Used in the Water Model

Casting speed (m/min)	1.0, 1.2, 1.4, 1.6, 1.8
SEN submergence depth (mm)	40, 70, 700, 130, 160
Gas flow rate (Nl/min)	0, 4.58, 9.16, 12.74, 18.32
SEN outport angle	+5 deg, –0 deg, –5 deg, –15 deg, –25 deg
Bore diameter of the SEN (mm)	30, 35, 40, 45, 50
Ports-to-bore area ratio ψ	1.5, 1.73, 2.0, 2.27, 2.5

C. *Computational Models*

After simulations of fluid flow and heat transfer in a cylindrical continuous casting mold with a straight nozzle were published in 1970 by Szekely *et al.*,[60] many investigations on fluid flow in the continuous casting mold have been conducted using mathematical models.[61–79] These fluid flow models have produced insights into the flow pattern in the nozzle[46,67,80–82] and mold,[25,34,83–87] including the effects of nozzle geometry,[36,44,46,67,88] argon gas injection,[18,80–82] impingement of the superheated steel jet onto the solidifying shell at the narrow face,[89] shape and fluctuations of the top surface level,[77,90–92] electromagnetic forces,[75,93] and inclusion entrapment.[78]

In the current article, three-dimensional fluid flow in the water model of the tundish, the SEN, and the mold is calculated with the k-ε turbulence model, using a single-phase Eulerian model of the liquid phase in Fluent.[94] The trajectories of many individual bubbles are predicted by considering the buoyancy and drag forces acting on the bubbles using an uncoupled Lagrangian model, which includes the effect of turbulent

Table III. Orthogonal Array $L_9(3^4)$: Nine Combinations for Four Factors with Three Values

Combination	Factor 1	Factor 2	Factor 3	Factor 4
1st	1	1	1	1
2nd	1	2	2	2
3rd	1	3	3	3
4th	2	1	2	3
5th	2	2	3	1
6th	2	3	1	2
7th	3	1	3	2
8th	3	2	1	3
9th	3	3	2	1

Table IV. Fluid Flow Pattern in the Water Model of the Mold

Strand Size	Casting Speed	Gas Flow Rate	SEN				Flow Pattern
			Submergence Depth	Outport Angle	Bore Size	Area Ratio ψ	
200 mm × 900 mm	1.0 m/min	4.6 Nl/min	70 mm	0 deg	35 mm	1.73	double roll
	1.2 m/min	4.6 Nl/min	100 mm	–15 deg	50 mm	1.5	single roll
	1.4 m/min	13.7Nl/min	40 mm	–5 deg	50 mm	1.73	single roll
	1.8 m/min	9.2 Nl/min	70 mm	+5 deg	50 mm	2.27	double roll
	1.8 m/min	13.7 Nl/min	100 mm	0 deg	30 mm	2.5	double roll
	1.8 m/min	18.3 Nl/min	130 mm	–5 deg	35 mm	1.5	double roll
200mm × 1250 mm	0.8 m/min	0 Nl/min	40 mm	+5 deg	30 mm	1.5	double roll
	0.8 m/min	9.2 Nl/min	100 mm	–5 deg	40 mm	2.0	single roll
	1.0 m/min	0 Nl/min	70 mm	–5 deg	45 mm	2.5	double roll
	1.0 m/min	4.6 Nl/min	100 mm	–15 deg	50 mm	1.5	single roll
	1.0 m/min	18.3 Nl/min	40 mm	0 deg	40 mm	2.27	single roll
	1.2 m/min	9.2 Nl/min	160 mm	0 deg	45 mm	1.5	double roll
	1.2 m/min	13.7 Nl/min	40 mm	–5 deg	50 mm	1.73	single roll

flow fluctuations with a Random-Walk model.[61,79] This approach is only reasonable for very small gas fractions, such as found when the only source of gas is argon leaking through the slide gate seals inside the SEN. Detailed equations can be found elsewhere.[79,86] For the simulation of fluid flow, a fixed velocity condition is imposed at the domain inlet, and a "pressure outlet condition" is used at the outlets. For simplicity, the top surface is assumed to be flat with no slag phase, and zero shear stress. Standard "wall functions" with zero velocity at the wall are used as boundary conditions in order to capture the steep gradients with reasonable accuracy on a coarse grid.[66,67,68] The bubbles are assumed to escape at the top surface and the mold bottom, and to be reflected at other walls.

D. *Plant Experiments*

Industrial trials and measurements in the actual steel plant are crucial to ultimately quantify the effects of casting variables on quality concerns, owing to the great complexity of the phenomena. High casting speed variations were observed to increase mold slag entrainment.[95] To decrease these problems, the top surface velocity should be kept below a critical maximum velocity, which has been estimated to be 0.3 m/s[48] or 0.4 m/s.[24] However, some minimal surface flow, including level fluctuations at the meniscus, is required in order to prevent quality problems such as meniscus freezing,[24,96] capturing of inclusions into the meniscus surface, and deep oscillation marks. For example, decreasing surface velocity below 0.4 m/s was measured to increase surface pinhole defects.[97] To avoid these problems, the flow pattern should be designed to exceed a critical minimum velocity across the top surface, estimated to be about 0.1 to 0.2 m/s.[24] Although the detrimental effect of level fluctuations is well known, only a few industrial measurements have quantified the effects.[19,77] Level fluctuations of 6 to 9 mm at the meniscus during continuous casting were reported to cause the fewest surface defects in cold-rolled coils.[19] This corresponds to optimal level fluctuations in the water model of this work of 3.6 to 5.4 mm using Eq. [4]. The waves and level fluctuations on the top surface in a water model were smaller than those in the steel caster, as predicted by Yuan and confirmed by comparison with measurements.[77] Fluid flow velocities in the steel caster were measured using electromagnetic sensors[98,99,100] and validated using water and computational models.[86] These experiments revealed the single-roll or double-roll nature of the flow pattern in the real steel casting mold.

In the current study, industrial trials are performed for a three-heat sequence (240-tonne total) cast with a slab size of 200 × 1250 mm, casting speed of 1.0 to 1.2 m/min. The purposes of the industrial trials are to check the effect of the optimized SEN configuration in the water model and the optimal operation conditions, such as the suitable argon gas injection. In the trials to investigate inclusions in steel, there is no gas injection. To trace the origin of inclusions caused by mold slag entrainment, La_2O_3 is added to the mold flux before casting. The caster has two strands: strand 1 is with the recess well SEN, and strand 2 is with the pointed-bottom SEN.

Molten steel samples are taken from the continuous casting mold at the ¼ width and 100 mm below the surface of the molten steel to analyze the total oxygen (TO) and the nitrogen. Great care was taken during sample collection to avoid contamination with liquid slag or air. This was accomplished using a sample collecting ladle with a closing lid. This sample ladle was inserted into the molten steel quickly and taken out after several seconds. The steel sample was then machined off the surface at the work shop and polished for later microscope observation and TO and N analysis.

Slab samples were sectioned and analyzed with an optical microscope to reveal and count typical inclusions. The schematic of sampling of the slab is shown in Figure 3. The complete size distribution including the rare large inclusions (> 50 μm) was determined with Slime tests,[101] which involved dissolving the steel away from the inclusions in 2-kg steel samples taken from solid slabs.

Liquid mold slag samples were taken to study the change in Al_2O_3 content during continuous casting. The

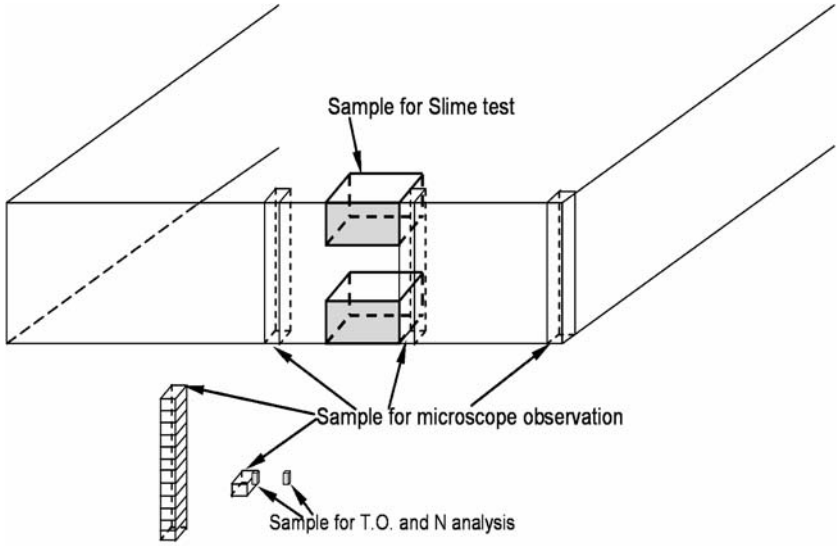

Fig. 3—Sampling places at continuous casting slab.

thickness of the liquid slag is measured at 10 mm from the narrow face, at the ¼ width centerline, and 10 mm from the SEN, by vertically inserting steel spikes into the molten steel and slag layer for several seconds.

III. FLOW IN THE NOZZLE

Three kinds of fluid flow pattern were observed in the SEN water model, as shown in Figure 4: bubbly flow (Figure 4(a)), annular flow (Figure 4(b)), and critical flow between these two (Figure 4(c)). For the ''bubbly flow'' pattern, the water, and the gas are well mixed, and the jets at the two outports are relatively uniform and symmetrical. Turbulence in the SEN is very strong, so both the liquid and gas phases have large energy losses, leading to a small jet energy and low impingement pressure at the narrow face. In addition, the strong interaction between the gas and the liquid in the SEN likely tends to dislodge any inclusions just attached to the SEN walls, which lowers the tendency for clogging.

For the ''annular flow'' pattern, the liquid annularly enters the SEN and then flows down along the walls, as it periodically changes its position. The liquid flow separates from the gas, which forms large pockets just below the stopper. The energy loss is small, so the impingement pressure to the narrow face is high. The flow is unstable, so the jets from the two outports tend to be asymmetrical. A given outport may emit more gas and less water, as the large gas regions escape and move intermittently along the outer walls of SEN to the top surface, where they rupture. This creates large level fluctuations and might contribute to the foam observed near the SEN.[30] At the other outport, there would be more water and less gas, giving the jet high momentum and speed, leading to high impingement pressure on the narrow face and large meniscus level fluctuations.

For the critical flow pattern, part of the inside of the SEN is bubbly flow and the rest is annular flow. A tiny change of the water height in the tundish, casting speed, or gas flow rate can switch this critical flow to annular flow or to bubbly flow. If the flow regime suddenly switches to annular flow, the resistance to flow increases, which causes the water height in the tundish to increase abruptly and the level in the mold to decrease abruptly. Water may even overflow the tundish. If the flow regime suddenly switches to bubbly flow, the resistance to flow

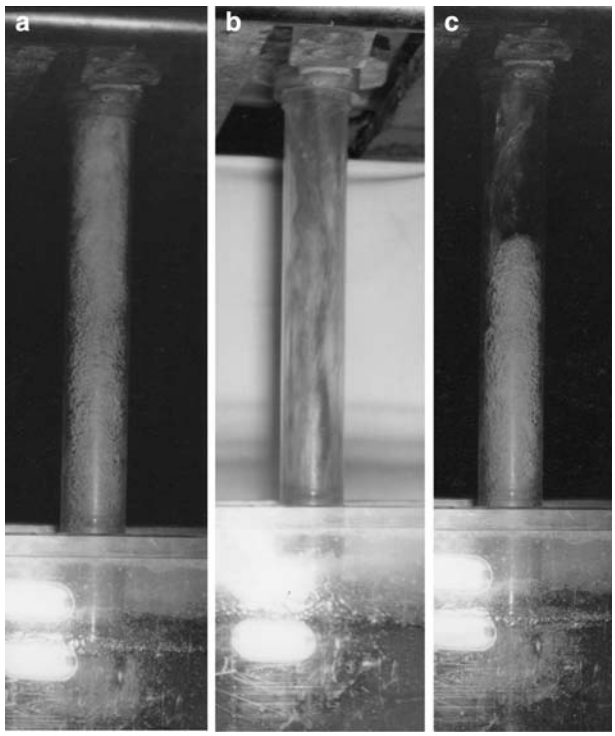

Fig. 4—The multiphase fluid flow pattern in the SEN with 45-mm bore diameter: (*a*) bubbly flow, (*b*) annular flow, and (*c*) critical flow.

decreases, which causes the water height in the tundish to decrease abruptly and the level in the mold to increase abruptly. Water may even overflow the mold. Clearly, this flow pattern is detrimental to steel quality. These findings agree closely with the observations in the SEN of annular and bubbly flow by Burty.[102,103,104]

This behavior is characteristic of nozzles with oversized ports, relative to the nozzle bore, which are chosen to provide tolerance to clogging. However, these ports produce very small pressure drops and provide minimal resistance to flow transients. They exhibit low velocity regions of back flow at the top of the ports (Figure 5 (b)), which is consistent with previous predictions for this port-to-bore ratio.[68,105] These regions are very susceptible to the intermittent gas bubble release that accompanies annular flow and causes asymmetric flow in the mold. The flow pattern in the SEN with a fixed-bore diameter is controlled by the liquid and gas flow rates and the pressure (which depends on tundish level). The bubbly flow pattern in the SEN is most likely at low gas flow rate and high liquid flow. As the casting speed is increased, the range of the gas flow rate required to maintain bubbly flow is also increased; in other words, with increasing casting speed, more gas can be injected into the liquid with achieving the bubbly flow pattern in the nozzle. For a given casting speed, there is a maximum gas flow rate to achieve bubbly flow. Beyond this maximum gas flow rate, the flow pattern in the nozzle will be annular flow, as shown in Figure 6. For example, if the water throughput is 6 m^3/h and the liquid height in the tundish is 600 mm, the gas flow rate should be smaller than 19.5 Nl/min for bubbly flow. Increasing the liquid height in the tundish allows a slightly greater gas flow rate to retain bubbly flow, with other conditions kept constant.

In the real steel caster, a bubbly flow pattern in the SEN is desired to prevent unstable and asymmetrical flow in the mold. The results in Figure 6 can be converted into the steel-argon system and related to casting speed by applying the similarity criterion (Eq. [5]) and the mass balance equation (Eq. [6]). Using Eqs. [7], [8], and [11], Figure 6 was redrawn into Figure 7 to suggest corresponding relations in the steel continuous casting process. It must be re-emphasized that these

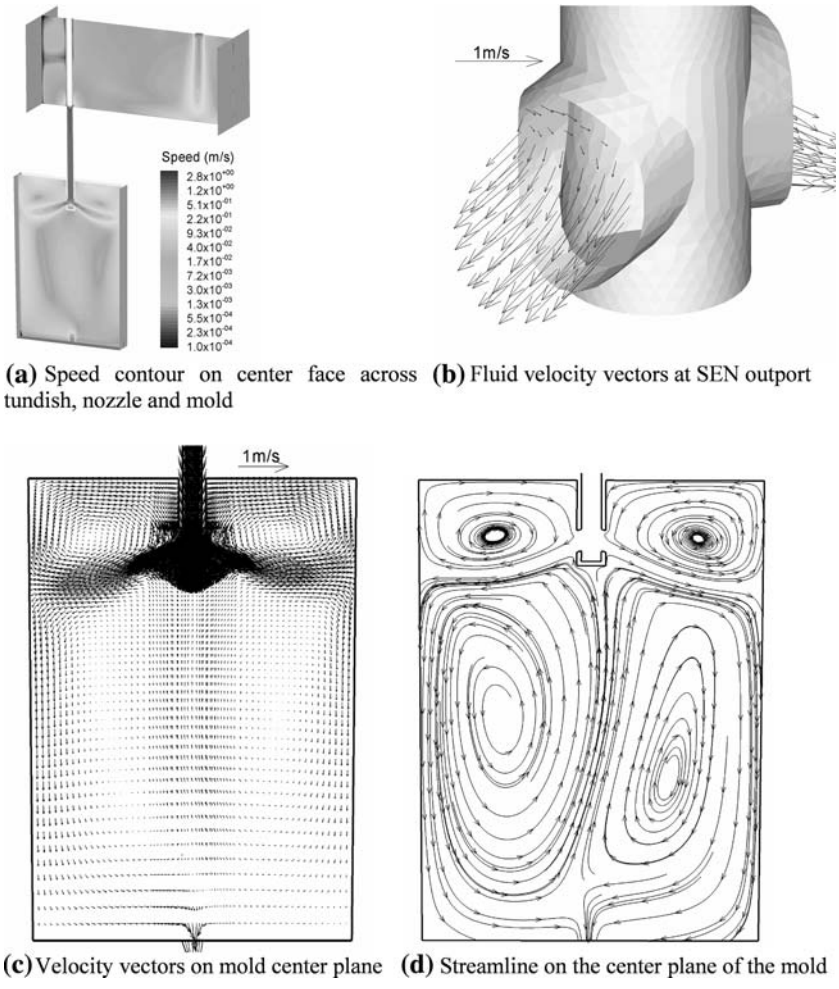

(a) Speed contour on center face across tundish, nozzle and mold **(b)** Fluid velocity vectors at SEN outport

(c) Velocity vectors on mold center plane **(d)** Streamline on the center plane of the mold

Fig. 5—Calculated single-phase fluid flow in the tundish, the SEN, and the mold (water model of the 200 mm × 1250 mold, casting speed: 1.4 m/min, tundish inlet velocity: 0.731 m/s, inlet turbulent energy: 0.004 m^2/s^2, its dissipation rate: 0.03 m^2/s^3, SEN bore diameter: 45 mm, outport angle: down 15 deg, submergence depth of the SEN: 130 mm, water height in the tundish: 600 mm, tundish length: 1400 mm, and tundish thickness: 400 mm).

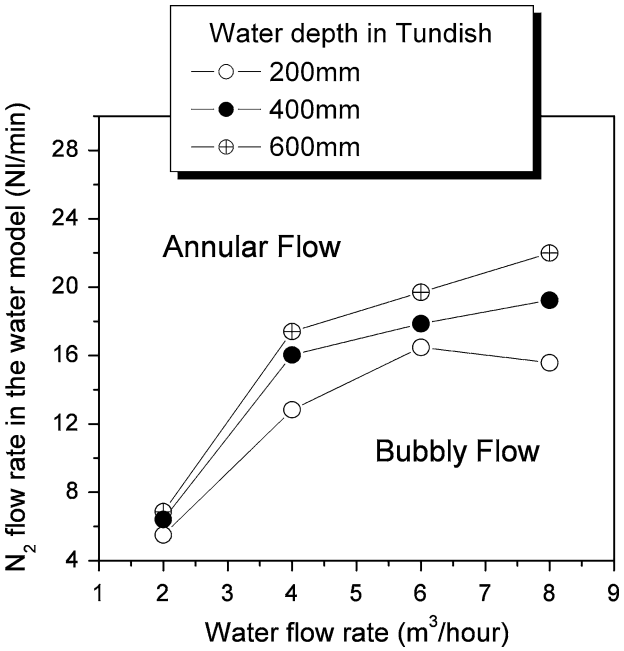

Fig. 6—Conditions to achieve annular flow or the bubbly flow in a 45-mm SEN (water model).

predicted flow regimes need validation with better computational models and plant experiments.

IV. FLOW IN THE MOLD

Two distinct types of flow pattern in the mold are single roll and double roll. Table III summarizes the single or double-roll flow patterns obtained in the water model resulting from different conditions. This work confirms previous findings that the single-roll flow pattern is more likely with high gas injection, small SEN submergence depth, and small casting speed.[18,106] The double-roll flow pattern is more likely with large casting speed, large SEN submergence depth, and small gas flow rate.[18,106]

With minimal argon gas injection, and oversized, downward-directed ports, the fluid flow pattern in the mold region of the Panzhihua caster is a typical "double-roll flow pattern." This is shown in the typical single-phase simulation results in Figure 5, which includes computations of fluid flow in the tundish, SEN, and mold regions. The jet impinges on the narrow face, where part of the flow moves upward along the narrow face to form the upper roll and another part flows downward to generate the lower roll (Figures 5(c) and (d)). The fluid flow is slightly asymmetrical, which is likely a convergence problem induced by the unstructured mesh used at the region of the SEN outports. Although this is a numerical problem, the actual flow pattern exhibited similar asymmetries, which are consistent with those observed elsewhere.[76] The calculated location of the upper roll is 0.13 m below the top surface, and the lower roll is 0.57 to 0.72 m below the top surface. In the water model measurements for these

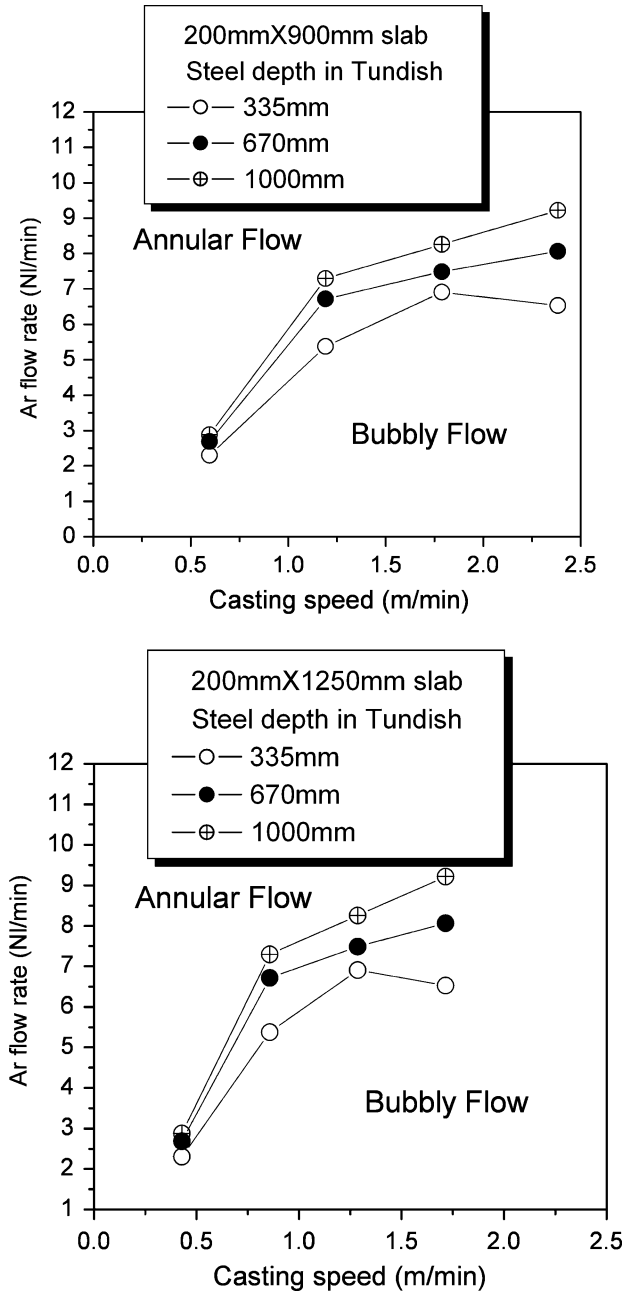

Fig. 7—Conditions to change annular flow to bubbly flow in a 75-mm SEN (liquid steel) for different size slabs.

conditions with no gas, the left low roll is located 0.61 mm below the top surface, roughly matching the simulation.

A. *Effect of Gas Flow Rate and Casting Speed*

The water model results in Figure 8 show that increasing casting speed with other variables held constant encourages the double-roll flow pattern. The flow patterns in Figure 9 show the same trend, with the complication that increasing gas flow rate was compensated by increasing submergence depth. In the single-roll flow pattern (a), the top surface level near the SEN is highest, whereas with the strong double-roll flow pattern

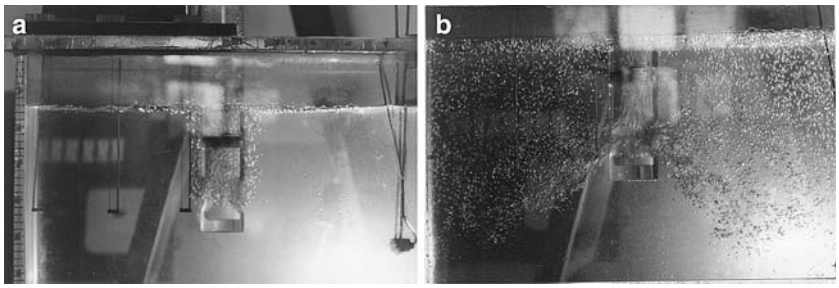

Fig. 8—Two-phase fluid flow pattern in the water model of the 200 × 1250 mm steel slab (bore diameter of the SEN: 45 mm, gas flow rate: 5.344 Nl/min, submergence depth of the SEN: 100 mm, and water flow rate: (*a*) 2.0 m^3/h and (*b*) 6.6 m^3/h).

(b), the level near the narrow face is highest. Note that for the low casting speed, bubbles leave the jet and move up along the outer SEN walls, according to their buoyancy. With excessive gas flow rates, this may emulsify the slag at the top surface near the SEN. The single-roll flow pattern also tends to increase top surface level fluctuations.

Excessive argon injection may generate transient variations of the jets entering the mold, introduce asymmetry in the mold cavity,[107] and increase surface turbulence. To maintain a stable double-roll flow pattern, which is often optimal,[98,100] the argon gas flow rate should be kept safely below a critical level.[98,99,108] The critical level depends on the casting speed, submergence depth, nozzle angle, and other flow parameters, which is consistent with previous work, discussed in detail elsewhere.[18,80–82]

B. *Lower-Roll Location*

Figure 10 shows the effects of process parameters on the depth of the center of the lower recirculation roll. This point becomes deeper with increasing casting speed and decreasing gas flow rate. These trends are the same as those favoring the double-roll flow pattern. In addition, the lower roll center becomes deeper with increasing submergence depth or decreasing SEN bore diameter.

V. TOP SURFACE MOLD LEVEL FLUCTUATIONS

Level fluctuations cause surface defects in addition to slag entrainment at the meniscus. Level fluctuations are mainly induced by jet impingement and upward flow along the narrow face, rupture of bubbles at the top of the liquid, a single-roll flow pattern in the mold, the gas injection, and the transient, asymmetric nature of turbulent flow itself. A typical trace of the level fluctuation recorded at ¼ point on the top surface of the water model is given in Figure 11, and divided into low and high frequency components by averaging the fluctuation with some time-step and subtracting the fluctuation with averaged value. The averaged value is the low frequency oscillation, as shown in Figure 11(b),

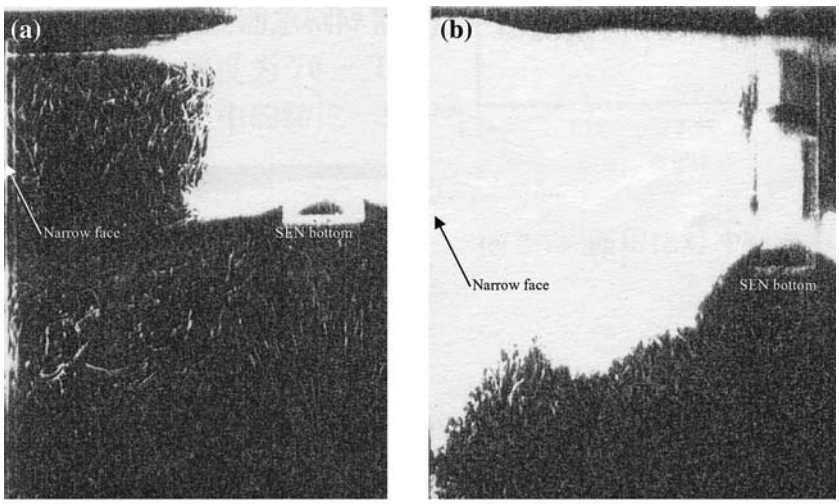

	Casting speed	Submergence depth of SEN	Gas flow rate	Outport angle of SEN	Bore size of the SEN	Port to bore area ratio ψ
(a)	1.2 m/min	100 mm	4.6 Nl/min	-15°	50 mm	0.67
(b)	1.8 m/min	130 mm	18.3 Nl/min	-5°	35 mm	0.67

Fig. 9—Fluid flow pattern in the 200 × 1250 mm mold progressing from (a) the single roll to (b) the double roll.

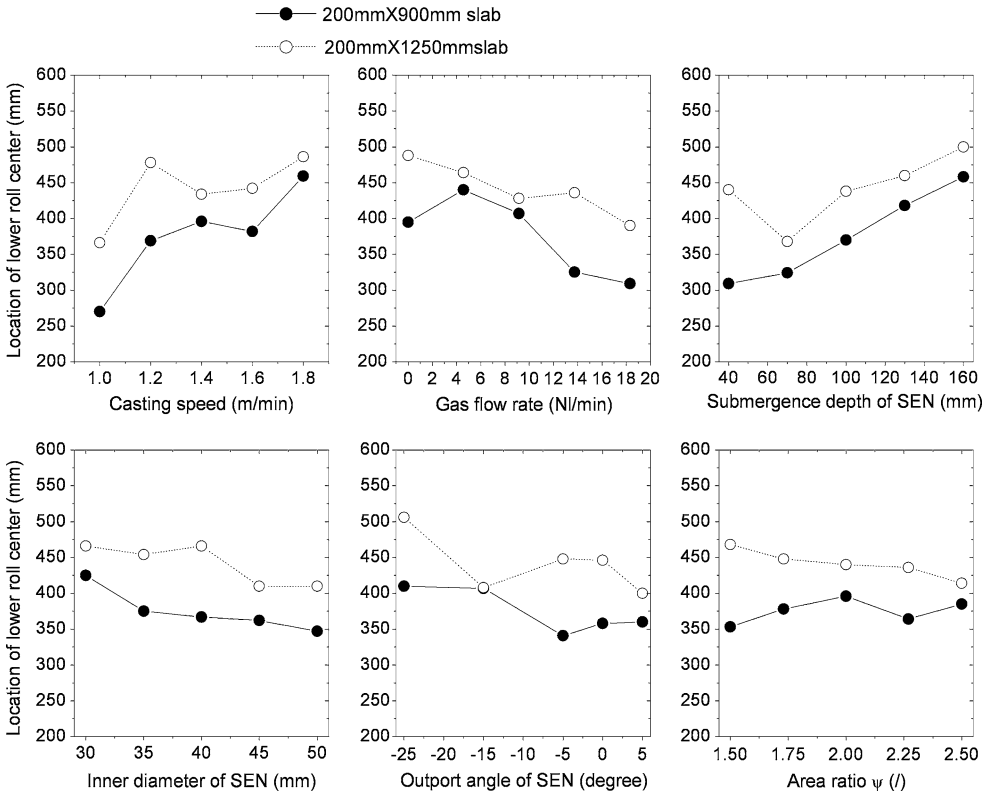

Fig. 10—Factors affecting the depth of the lower roll center.

which stems from the asymmetrical flow.[28,109] The high frequency fluctuation (Figure 11(c)) is mainly generated by the chaotic nature of the turbulence.[68] The amplitude of the low and high frequency components is similar, around ± 5 mm. However, the longer duration of the low frequency oscillation likely makes this component worse for causing quality problems.

The effects of different process conditions on the average maximum level fluctuation at different locations across the top surface centerline of the water model are shown in Figures 12 through 17. These figures include variations owing to changes in other variables besides those indicated. All of the results indicate that the level fluctuations at the meniscus near the narrow face are smaller than those in the interior (centerline) at the quarter-width locations or near the SEN. They also indicate that level fluctuations for the 900-mm width are larger than for the 1250-mm width.

A. *Effect of Gas Flow Rate and Casting Speed*

Level fluctuations at the meniscus increase with increasing gas flow rate, as the flow pattern tends to single roll (Figure 12). When the casting speed is low, or the gas flow rate is high, the gas mainly exits the top surface near the SEN (Figure 8(a)), so level fluctuations are worse near the SEN. With high casting speed, the bubbles follow the jet further and tend to exit closer to the narrow face, where the largest level fluctuations are then found. For the same conditions, the smaller width slab has larger level fluctuations. This might be because the turbulent energy is more easily dissipated in the larger volume. For the same conditions, the meniscus region generally has smaller level fluctuations than the interior of the top surface. To obtain 3.6- to 5.4-mm level fluctuations at the narrow face meniscus, the gas flow rate for the 1250-mm-width slab should be within 5.3. to 6.9 Nl/min, and for the 900 mm width slab, the gas flow rate should be within 4.6 to 7.6 Nl/min.

Past work has found that a larger casting speed tends to induce larger level fluctuations at the meniscus.[100] In this work, however, casting speed has no clear effect on the level fluctuations (Figure 13), due to compensating changes in the flow pattern. Increasing speed tends to switch from a single- to a double-roll flow pattern, which decreases surface velocities. This tends to offset the general increase in surface velocity caused by the higher speed. Moreover, flow stability and transient oscillations, which are most responsible for level fluctuations, are not directly related to speed when gas is present.

B. *Effect of Submergence Depth*

Level fluctuations at the meniscus decrease with increasing submergence depth to about 70 mm (Figure 14). Further increasing the submergence depth beyond 100 mm switches to increasing the level fluctuations. The reason for this small effect is the change from single- to double-roll flow pattern with increasing submergence depth. The best submergence depth is around 70 to 100 mm, which produces 5.1-mm level

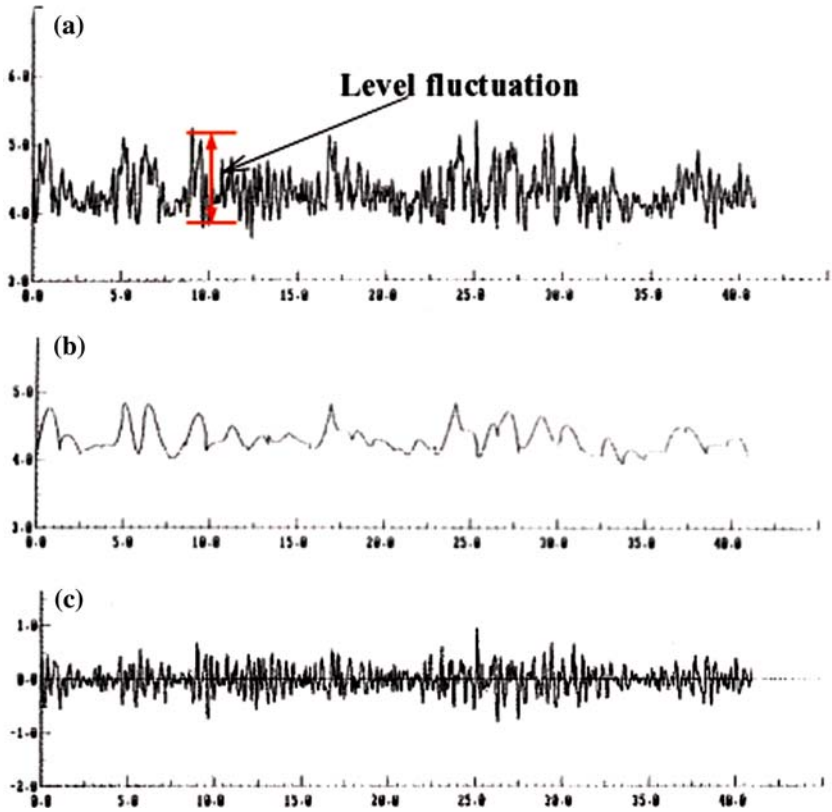

Fig. 11—(*a*) Example of the measured level fluctuation signal (*b*) split into low frequency and (*c*) high frequency components.

fluctuation at the meniscus for the 1250-mm width and 5.7 mm for the 900-mm width.

C. *Effect of Nozzle Geometry*

Figure 15 shows that the SEN outport angle should be downward 5 to 15 deg, because level fluctuations increase for angles outside of this range. Increasing angle tends to generate the single-roll flow pattern, which has larger level fluctuations. Too large a downward angle may enhance flow pattern asymmetry, with corresponding large level fluctuations.

As shown in Figure 16, the level fluctuations decrease with increasing bore diameter of the SEN. This is likely due to decreasing the size of the channel between the SEN outer bore and the mold walls, which lowers surface velocity there. This prevents communication between the two sides of the mold, which tends to discourage flow asymmetry and the associated level fluctuations. The larger bore diameter of SEN also affects the fluid flow pattern in the SEN. With a larger bore, the fluid flow velocity in the nozzle is smaller. Thus, the jet into the mold has smaller energy, decreasing the level fluctuations.

The optimal inner diameter of the SEN is 45 mm, and the optimal ports-to-bore ratio is 2.27 for both the 900- and 1250-mm widths (outer diameter = 65 mm, keeping thickness 10 mm). With this bore size, the level fluctuations at the meniscus are 7.27 mm for the 900-mm width and 5.32 mm for the 1250-mm width.

Figure 17 shows that the level fluctuations decrease slightly with increasing the ports-to-bore area ratio ψ. This might be due to lowering the exit velocity. However, if the area ratio is too large, it likely causes more asymmetrical flow.

VI. NARROW FACE IMPINGEMENT PRESSURE

Figure 18 shows the effects of some parameters on jet impingement pressure to the narrow face. For the 900-mm width, the impingement pressure increases with increasing casting speed and decreasing inner diameter of the SEN. The impingement pressure is smallest for the 900-mm width if the gas flow rate is 9.2 Nl/min, the outport angle is downward 15 deg, and the submergence depth is 100 mm. If the area ratio is smaller than 1.75, the impingement pressure decreases with increasing area ratio. For the same conditions, the impingement pressure for the 1250-mm width is smaller than for the 900-mm width. For the 1250-mm width, the impingement pressure is independent of the submergence depth and the bore diameter of the SEN.

VII. IMPROVED RECESS-BOTTOM SEN DESIGN

Careful study of the fluid flow results reveals that no nozzle design is best for all casting conditions or for all

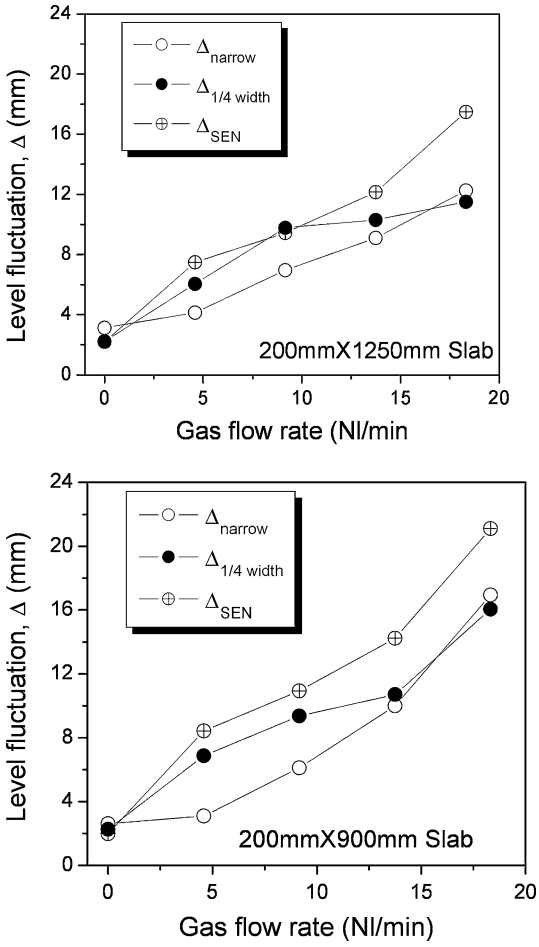

Fig. 12—Level fluctuations with different gas flow rates and mold widths.

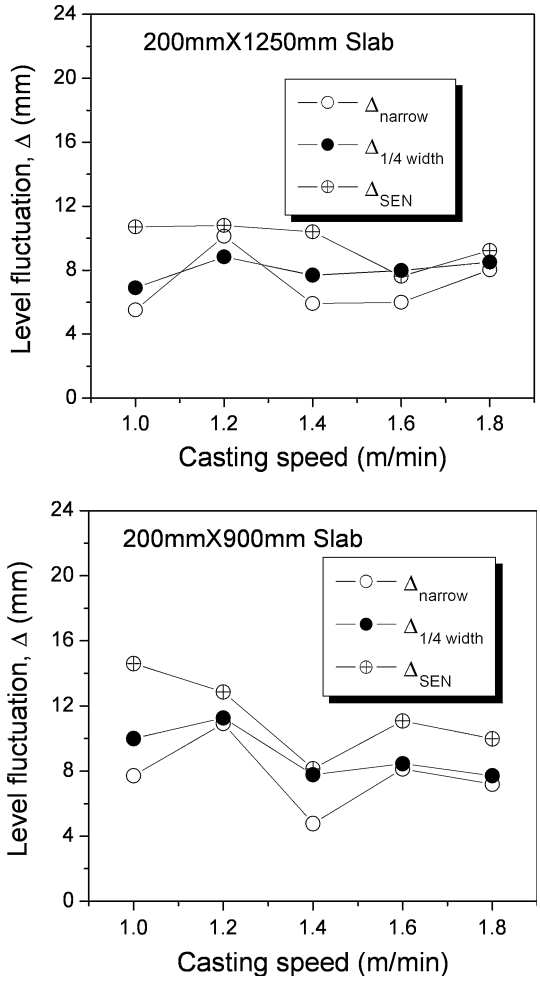

Fig. 13—Effect of casting speed on the level fluctuations.

attributes of the flow pattern. Nevertheless, an improved nozzle design was chosen and casting conditions were restricted according to the slab width. The common compromised recess-bottom SEN configuration chosen for the water model was 45-mm inner bore diameter, downward 15 deg 90-mm submergence depth, and 2.27 area ratio. For the real steel caster, this corresponds to a 75-mm-diameter inner bore, with 150-mm submergence depth.

For the continuous casting of 200 mm × 900 mm slabs, the casting speed is restricted to 1.4 to 1.5 m/min. The best gas flow rate for these conditions is 4.58 Nl/min in the water model, or 1.92 Nl/min in the steel caster. For the 200 × 1250 mm slabs, the casting speed is restricted to 1.2 to 1.3 m/min. The best range of gas flow rates is 5.34 to 6.87 Nl/min for the water model, or 2.24 to 2.90 Nl/min for the steel caster. From Figure 6, these casting speeds and gas flow rates should generate bubbly flow in the SEN.

VIII. EFFECT OF SEN BOTTOM WELL ON FLUID FLOW IN THE MOLD

Before this project, the current steel plant uses the traditional pointed-bottom-well SEN during continuous casting pouring. Water model experiments with the 200 × 1250 mm mold were performed with this pointed-bottom SEN and the optimized recess-bottom SEN configuration with 4.6 Nl/min gas flow rate and 90-mm submergence depth. The measured level fluctuation, the impingement depth, and the location of the lower roll center are shown in Figure 19. For the pointed-bottom SEN, the level fluctuations are generally smaller, which may not provide enough heat transfer to the meniscus. However, it has larger level fluctuations near the SEN at low and high casting speeds, owing to being prone to flow asymmetry. Finally, the pointed-bottom SEN has larger impingement pressure and greater impingement depth, which is not good for inclusion removal in the mold. Although this study is somewhat inconclusive, the recess-well SEN appears to be superior.

IX. GAS BUBBLE ENTRAPMENT

At optimal levels, bubbles injected into the nozzle are helpful by reducing nozzle clogging, lifting the fluid flow pattern to encourage inclusion removal, decreasing the

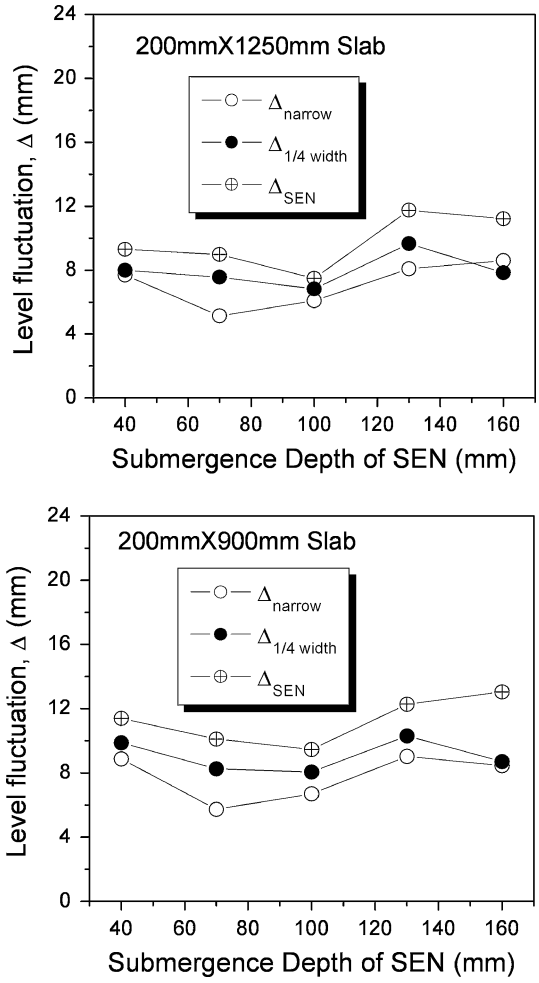

Fig. 14—Effect of submergence depth on the level fluctuation in the mold.

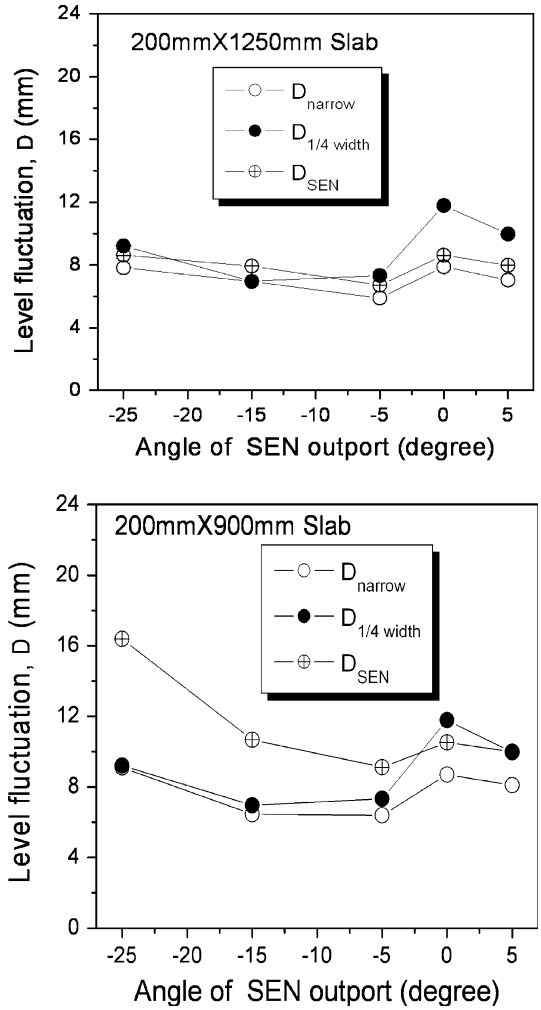

Fig. 15—Effect of SEN outport angle on the level fluctuation in the mold.

impingement pressure at the narrow face, and capturing inclusions as they flow in the liquid.[30,110–112] However, if the casting speed is too large or the gas flow rate is too high, some bubbles, especially those with many entrapped solid oxide particles, may be captured by the solidifying shell, eventually leading to surface slivers or internal defects.[30] Bubbles may also be entrapped at the meniscus, especially if large oscillation hooks or large level fluctuations occur.

The calculated trajectories of 10 typical bubbles with (a) and (b) 1-mm and (c) and (d) 5-mm-diameter in the single-phase water mold of Figure 5 are shown in Figure 20. Very rarely, a large bubble may penetrate deep and be entrapped through the bottom outlet. More of the 1-mm bubbles leave the outlet at the mold bottom. The bubble motion in the mold is very chaotic, varying from symmetrical to asymmetrical, which corresponds with transient biased flow in the mold.

X. INDUSTRIAL MEASUREMENT OF INCLUSION ENTRAPMENT

The purpose of the water modeling and mathematical simulation is to provide useful information to guide the real steel continuous casting industrial operation. Industrial trials are very important due to the following reasons.

1. The industrial experimental results serve to validate the water model predictions, by providing feedback on the fluid flow phenomena in the mold. In water modeling, the surface fluctuation in the mold poured by different SENs is reported (Section VIII and Figure 19): the optimized recess-well SEN by water models and the traditional pointed-bottom SEN. In the plant trials, the effects of these two types of SENs on inclusion content in steel are compared. Fluid flow in the real steel continuous casting mold was also observed, especially the top slag layer fluctuation under different gas injection flow rates. This phenomenon has been investigated in the water modeling (Sections III and IV). Plant trials were conducted to estimate the fluid flow pattern in the mold and to compare the steel cleanliness of cast slabs poured using the optimized recess-well SEN by water models with that using traditional pointed-bottom SEN, and also were

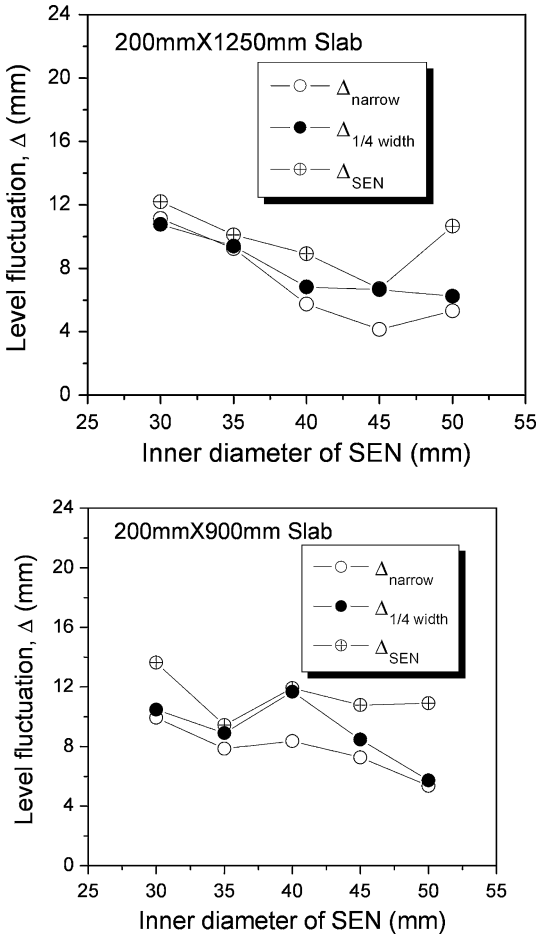

Fig. 16—Effect of inner bore diameter of SEN on level fluctuations in the mold.

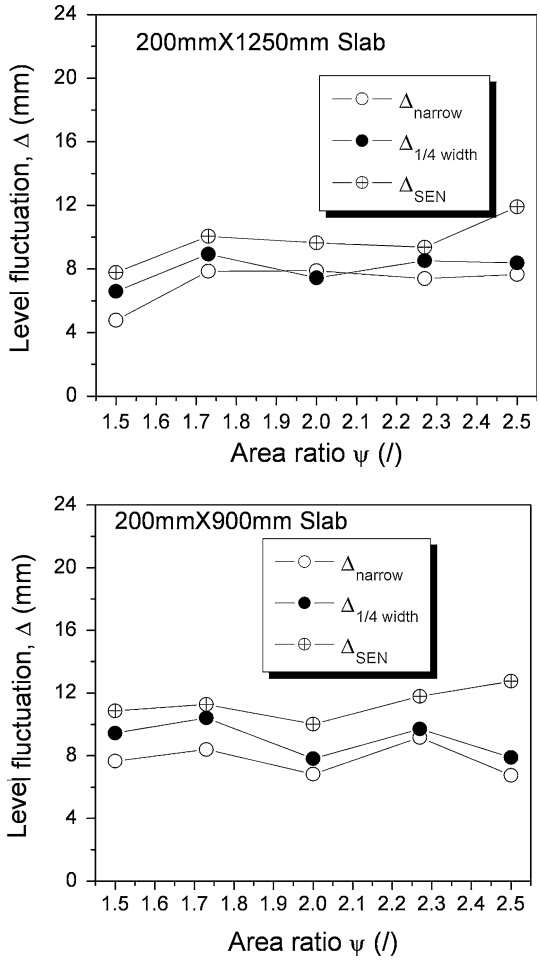

Fig. 17—Effect of port-to-bore area ratio ψ on mold level fluctuations.

performed to observe and quantify the amount of inclusions captured in the solid steel strand, compared to those removed safely into the top slag layer. At the two-strand caster in the current study, strand 1 uses the recess-well nozzle and strand 2 uses the traditional pointed-bottom nozzle.

2. Very few quantitative plant measurements are reported in the literature, which include observation and measurements to provide accurate determination of steel cleanliness, including the expensive, time-consuming Slimes tests, which use a significant volume of materials (more than ten samples of ~1 kg each). These tests are better than typical spot-analysis or metallographic examination of sections, *etc.*, because they are able to find the rare large inclusions. The figures presented show clearly both what these large inclusions look like and how many appear in the product. Such inclusions are common in many plants, but are rarely discovered or published, owing to the difficulty of finding them.
3. Other novel plant measurements are reported to supplement the inclusion measurements, including observations of flow in the mold, inclusion absorption on the top surface, and inclusion entrapment into the final solidified steel.
4. In addition to being novel, unique, important results in their own right, this experimental work augments the results obtained from water modeling and computational modeling.

In order to obtain a true understanding of an industrial process, it is crucial to have a combination of modeling (for understanding) and plant experiments (to prove that the models are truly relevant). Even better is to have computational modeling, water modeling, and plant experiments together sending a coherent message.

A. *Fluid Flow Pattern in the Mold with Gas Injection*

According to Figure 7, for the casting of 200×1250 mm steel slabs at 1.1 m/min casting speed with 1000-mm steel height in the tundish, the argon gas flow rate should be below 6.5 Nl/min to get the bubbly flow pattern in the SEN. However, in the previous continuous casting operations with pointed-bottom SEN, the gas flow rate used prior to this study was 10 to 20 Nl/min, which is predicted in Figure 7 to produce annular flow in the SEN, inducing biased flow in the mold, serious level fluctuations, and slag entrainment. Indeed, chaotic fluctuations, somewhat periodically,

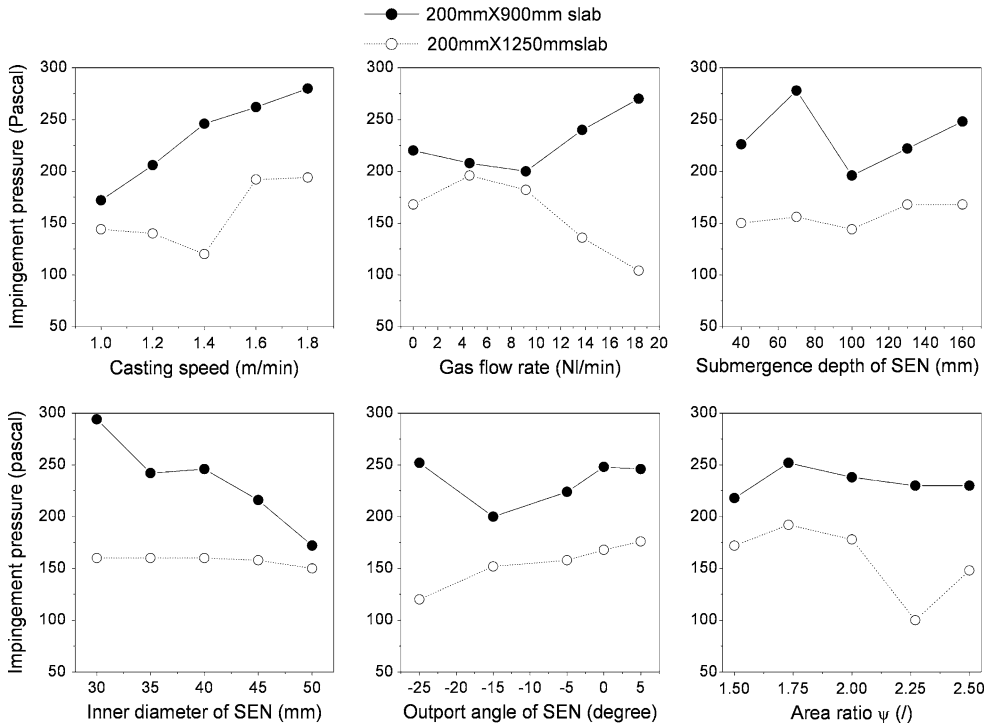

Fig. 18—Factors affecting the impingement pressure.

were observed beneath the surface of the slag layers in the steel caster, especially at the ¼ width of the mold. Somewhat periodically, "jumping" of the flux, or burning of the mold flux (as shown in Figure 21[113]), even accompanied by opening of an "eye" or bare spot on the top surface of the molten steel with no slag cover, could be observed. This detrimental flow state is termed "jumping of the fish" and is induced by the transient and asymmetry flow pattern in the entire mold. After changing to a new recess-bottom SEN configuration optimized by the water model and lowering the gas flow rate to the bubbly flow regime below the line in Figure 7, this phenomenon was diminished. During times such as ladle changes, when the tundish height and casting speed decrease, the gas flow rate must drop greatly to satisfy this criterion and maintain bubbly flow in the SEN.

Asymmetrical variations in the transient flow structure in the mold are important because they may be linked with observations of inclusion entrapment from side to side;[12,114] they also may induce the serious top slag fluctuation, and the jumping of fish flow, as discussed in Section III and Figure 21. The associated asymmetrical surface velocities induce vortices at the top surface. In the water model, the vortex location was observed to move periodically with time. This asymmetrical flow could be induced by both (1) operational and (2) natural causes.

(1) Operation Conditions:

(a) off-center stopper rod, and off-center gas injection from the stopper rod;
(b) off-center positioning of the SEN in the mold;
(c) uneven bottom shape of the SEN due to manufacturing, erosion, or clogging problems;
(d) asymmetrical shape of the two ports including the port diameter and port angle;
(e) asymmetrical gas injection through the slide gate, or porous brick of the SEN; and
(f) changes in casting speed or gas flow rate, such as during ladle changes.

(2) Natural cause of fluid flow asymmetry in the SEN and mold:

(a) asymmetrical clogging of the nozzle causing asymmetric flow;
(b) asymmetrical inflow due to flow across the bottom well of the tundish;
(c) chaotic nature of turbulence of the fluid flow in the mold;[38,115] and
(d) transient flow oscillations induced by the gas injection, such as annular flow (Figure 4).

The natural causes are suspected to be more important. To minimize the detrimental asymmetries caused by flow transients, it is important to address the preceding problems, in addition to designing the flow system to be resistant to asymmetries. It is also important to maintain a constant liquid steel level in the mold, constant powder feeding rate, constant casting speed, constant gas injection fraction,[81] constant slide gate opening, and fixed nozzle position (alignment and submergence). The transient flow and asymmetrical fluid flow in the mold need to be further investigated in detail in the future.

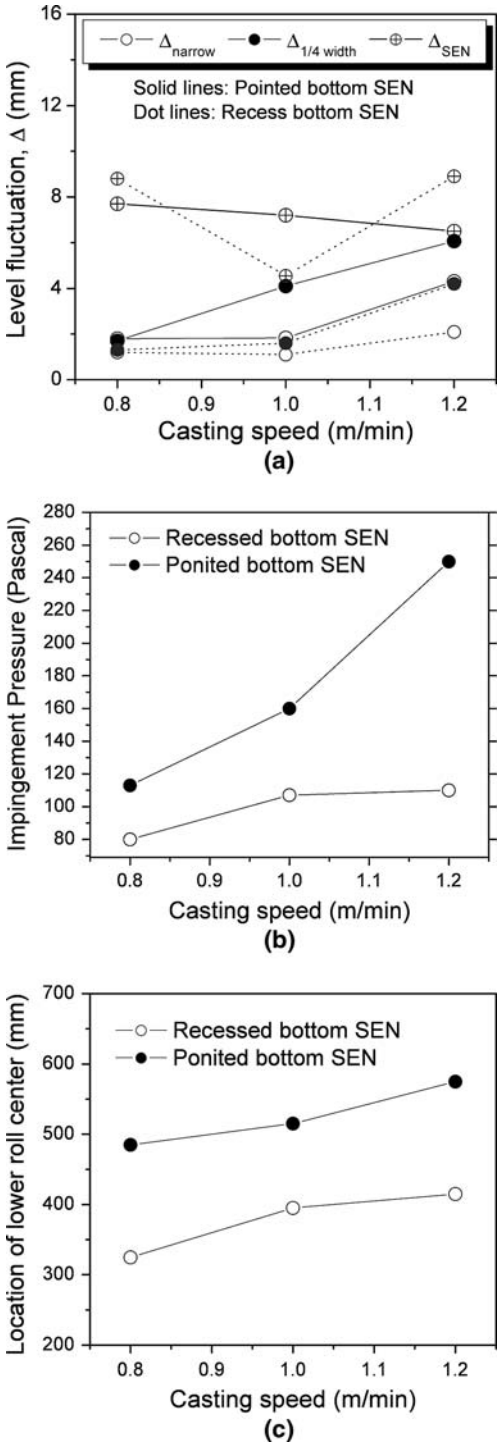

Fig. 19—(a) Measured level fluctuation, (b) impingement pressure, and (c) location of the lower roll center with different SEN bottom shapes for the water mode of the 200 × 1250 mm steel mold.

B. *Inclusion Observation*

Figure 22 shows typical large inclusions in the slab, extracted from the residue of the slimes tests, of samples taken from the ladle change casting period. Many of the particles contain La_2O_3 tracer (Table V), indicating mold slag. Most of these slag inclusions are also spherical, which indicates that they were liquid when captured by the steel. This demonstrates that mold slag entrainment is a serious problem during continuous casting. This confirms the importance of the efforts here to improve steel cleanliness, which focus on optimizing the mold flow pattern to decrease mold slag entrainment.

Microscope observations at ~300 separate fields (0.3-mm-diameter each field), per sample, were used to quantify the ratio of inclusion area to steel area in five samples, taken during steady casting. The results given in Table VI show that strand 2 (pointed-bottom SEN) had ~13 pct more inclusions (lower cleanliness) than strand 1 (recessed nozzle).

C. *Liquid Slag Layer Analysis*

The measured thickness of the liquid flux layer is shown in Table VII. The liquid flux at the narrow-face meniscus is 1- to 3-mm thicker than that at the ¼ width and near the SEN. The recess-well SEN generates 3 mm more liquid flux thickness than the pointed-bottom SEN. POSCO reported that for low-carbon Al-killed steel, if the casting speed is 1.0 to 1.6 m/min, the best thickness of the liquid slag layer should be 10 to 15 mm.[116] In the current investigation, strand 2 (pointed-bottom SEN) had insufficient slag layer thickness. This could disrupt meniscus solidification, leading to deep hooks, which can capture bubbles and inclusions. This might explain the lower cleanliness observed for the pointed-bottom SEN.

The absorption of alumina inclusions from the molten steel into the liquid flux on top of the mold has two components: (1) increasing the Al_2O_3 content from the mold powder composition (2.84 pct Al_2O_3) to the measured alumina concentration at steady state and (2) maintaining that value as flux is consumed.

The mass of the liquid slag layer, W_{LS} (in kg), can be calculated by

$$W_{LS} = S \cdot h \cdot \rho_{\text{slag}} \qquad [12]$$

where S is the cross-sectional area of the strand (0.2×1.25 m^2), h is the thickness of the liquid slab layer (m, in Table VII), and ρ_{slag} is the density of the slag, 3500 kg/m^3.

The Al_2O_3 inclusions removed to the liquid layer of the top slag at the mold can be calculated by $W_{Al_2O_3}$(in kg):

$$W_{Al_2O_3} = \frac{W_{LS} \cdot \Delta Al_2O_3}{100} \qquad [13]$$

where ΔAl_2O_3 is the increment of Al_2O_3 in the slag in percent (Table VIII).

The Al_2O_3 inclusions removed to all the slag, $M_{Al_2O_3}$ (in kg), can be estimated by

$$M_{Al_2O_3} = \frac{M_{\text{slag}} \cdot W_{\text{steel}} \cdot \Delta Al_2O_3}{100} \qquad [14]$$

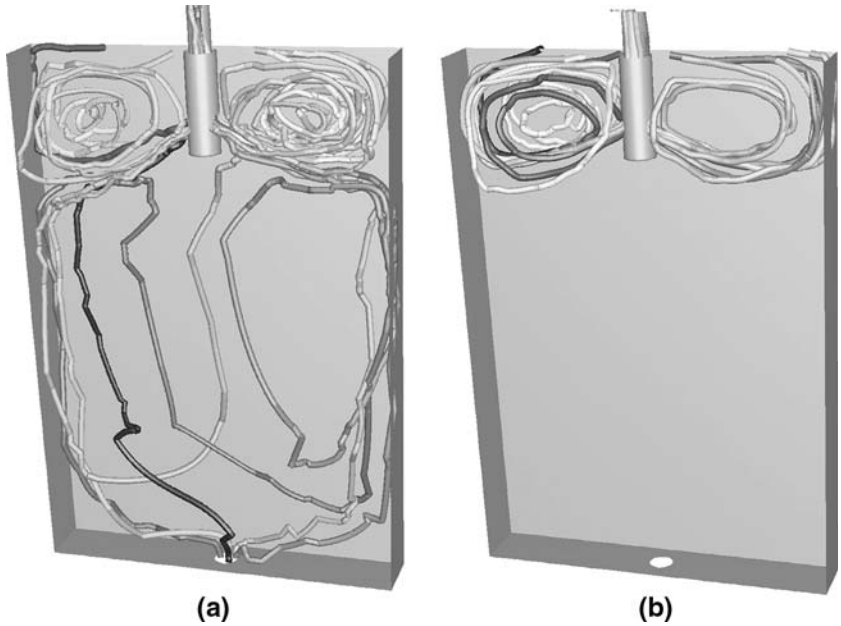

Fig. 20—Typical random walk trajectories of ten bubbles with the size of (a) 1 mm and (b) 5 mm in the mold water model of Fig. 5.

where M_{slag} is mold flux consumption, 0.5 kg/tonne steel here, and W_{steel} is the total molten steel poured per strand, 120 tonne here.

The TO removed at the mold, ΔO (ppm), can be represented by

$$\Delta O = \frac{(W_{Al_2O_3} + M_{Al_2O_3}) \times \frac{48}{102}}{W_{steel} \times 1000} \times 10^6 \qquad [15]$$

Based on the measured liquid flux thickness (Table VII), the mass of the liquid slag layer is 11.20 kg (strand 1) and 9.01 kg (strand 2), calculated by Eq. [12]. This corresponds to 0.492 kg of Al_2O_3 from the steel (strand 1) and 0.473 kg (strand 2) calculated by Eq. [13]. Next, based on the mold flux consumption rate of 0.5 kg/tonne, and total of 120 tonnes of steel cast per strand during the sequence, the total liquid slag consumed from the top surface is 60 kg per strand. By Eq. [14], Al_2O_3 inclusions removed to all the slag are of 2.634 kg (strand 1) and 3.150 kg (strand 2). Dividing the total increase (3.126 kg for strand 1 and 3.623 kg for strand 2) over the entire heat (120 tonnes per strand) and converting from alumina (102 g/mol) to oxygen (48 g/mol) with Eq. [15] gives 12.3 ppm TO removed from the steel (strand 1) and 14.2 ppm (strand 2). The results are given in Table IX.

Fig. 21—Burning of the mold flux at 1/4 width of the mold top surface during the slab casting process.[113]

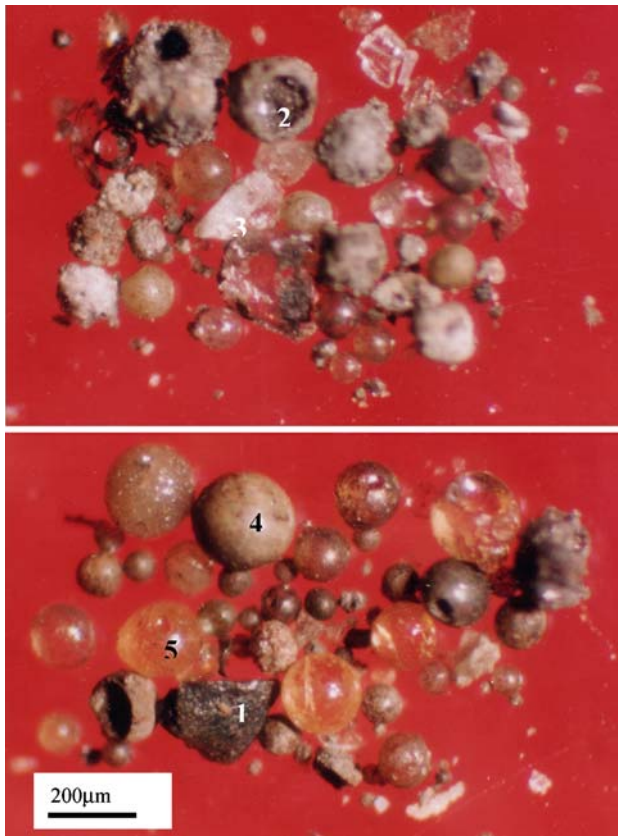

Fig. 22—Typical large inclusions in the slab extracted by the slime method.

Table V. Composition of Typical Large Inclusions in the Slab from Mold Slag Entrainment

1	Al_2O_3 40.11 pct, CaO 33.70 pct, SiO_2 20.02 pct, Na_2O 4.62 pct, La_2O_3 1.56 pct
2	Al_2O_3 65.30 pct, FeO 26.49 pct, CaO 2.1 pct, SiO_2 2.84 pct, MnO 0.85 pct, TiO_2 0.30 pct, BaO 0.13 pct, La_2O_3 0.065 pct
3	Al_2O_3 76.49 pct, FeO 13.82 pct, CaO 3.2 pct, SiO_2 3.47 pct, MnO 0.28 pct, TiO_2 0.06 pct, BaO 0.25 pct, La_2O_3 0.13 pct
4	Al_2O_3 2.86 pct, FeO 6.79 pct, CaO 0.18 pct, SiO_2 87.26 pct, MnO 0.15 pct, TiO_2 0.26 pct, BaO 0.94 pct, La_2O_3 0.49 pct, Na_2O 0.40 pct, K_2O 1.12 pct
5	Al_2O_3 2.38 pct, FeO 1.23 pct, CaO 4.47 pct, SiO_2 80.07 pct, MnO 0.03 pct, TiO_2 0.13 pct, BaO 0.55 pct, La_2O_3 0.65 pct, Na_2O 9.27 pct, K_2O 1.96 pct

Table VI. Area Percentage (Percent) of Inclusions by Microscope Observation

Samples	1	2	3	4	5	Mean
Strand 1	0.1789	0.1994	0.0890	0.0508	0.0481	0.11324
Strand 2	0.1991	0.1906	0.1083	0.0764	0.0786	0.1306

Table VII. Measured Thickness of Liquid Slag Layer on the Top of the Mold (mm)

	Near the Meniscus	¼ Width	Near the SEN	Mean Thickness
Strand 1	14	13	12	12.8
	14	11	10	
	15	13	13	
Strand 2	11	10	10	10.3

Table VIII. Measured Al_2O_3 Fraction in the Liquid Flux of the Mold (Initial Al_2O_3 Content in the Flux: 2.84 Percent)

	Al_2O_3 Fraction in the Liquid Slag (Pct)				ΔAl_2O_3 in Liquid Slag (Pct)
	Heat 1	Heat 2	Heat 3	Mean	
Strand 1	9.08	6.89	5.71	7.23	4.39
Strand 2	7.73	7.35	9.19	8.09	5.25

Table IX. Estimated TO Removal from the Steel by SEN and the Mold

	h (m)	W_{LS} (kg)	ΔAl_2O_3 (Pct)	$W_{Al_2O_3}$(kg)	$M_{Al_2O_3}$(kg)	Δ[O] (ppm)
Strand 1	12.8	11.20	4.39	0.492	2.634	12.26 ppm
Strand 2	10.3	9.01	5.25	0.473	3.15	14.21 ppm

D. *TO and Slime Test Analysis of Steel Slabs*

The mean of the TO of the molten steel in the mold of strand 1 is around 59 ± 35 ppm (Figure 23). It is assumed that the TO in the tundish entering both strands has similar TO values. Then, inclusion removal is 20.8 pct from strand 1 and 24.1 pct from strand 2, based on the estimation of TO removed to the top slag. This inclusion removal fraction by the mold slag agrees with the measured and simulated fractions of inclusions removed in the mold of a different 250×1300 mm caster using a different measurement method.[114] Moreover, in strand 1, the TO based on this inclusion mass balance is estimated to be $(59 \pm 35) \times (100 \text{ pct} - 20.8 \text{ pct}) = 46.7 \pm 28$ ppm, which matches well with the simple TO measurement of 47 ± 20 ppm in a slab from this strand. The greater inclusion removal fraction from strand 2 might be due to statistical variations, or it might indicate that mold slag entrainment is an important source of inclusions (not accounted for in this rough calculation) that is a more serious problem for the pointed-bottom nozzle.

The steel cleanliness is complicated greatly by the variations that occur during startup, ladle change periods, and end of casting. This is investigated for the two SEN bottom shapes by measuring the TO and nitrogen in the molten steel in the mold as a function of casting time and the amount of large inclusions in the slab extracted by the Slime method. The results, given in Figure 23, show that there is an abrupt increase in inclusions at the time of each ladle change. This might be aggravated by reoxidation from air absorption, slag entrainment in the tundish (due to emulsification during ladle opening or due to the lower tundish level), asymmetrical fluid flow from annular flow in the SEN induced by the low casting speed, and other reasons. Furthermore, the start and end of casting have almost

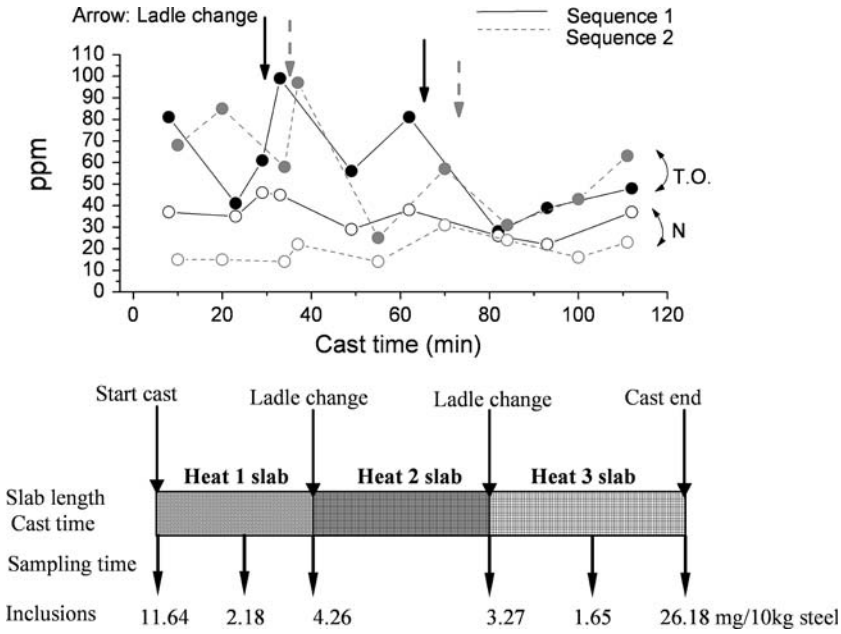

Fig. 23—TO and nitrogen content in the mold (upper figure) and > 50-μm inclusions in the slab by the slime test (lower figure).

tenfold more inclusions than during steady casting. This is when the preceding air absorption and slag entrainment phenomena are the most extreme. The period of the ladle change (3.3- to 4.3-mg inclusions per 10-kg steel) has twice the cleanliness problem of steady-state pouring (1.6- to 2.2-mg inclusions per 10-kg steel). Solving the cleanliness problems that occur during process transients is clearly an important task.

XI. CONCLUSIONS

In the current article, multiphase fluid flow and particle motion in the SEN and the mold of the slab continuous caster at Panzhihua Steel are investigated using water models, numerical simulations, and industrial measurements. In a 0.6-scale water model, designed according to the Weber–Froude similarity criterion, the top surface level fluctuations, the jet impingement pressure, and the flow pattern in the SEN and the mold are measured. The effects of SEN geometry, submergence depth, mold width, casting speed, and gas flow rate are investigated. Three kinds of fluid flow pattern are observed in the SEN: bubbly flow, annular flow, and an intermediate critical flow structure. The annular flow structure induces detrimental asymmetrical flow in the mold. Moreover, its higher resistance to flow makes switching between flow structures prone to level fluctuations, which is even more detrimental. The SEN flow structure depends on the liquid flow rate, the gas flow rate, and the liquid height in the tundish. The gas flow rate should be adjusted with changes in the casting speed in order to maintain stable bubbly flow.

Two main flow patterns are observed in the mold: single roll and double roll. The single-roll flow pattern is generated by large gas injection, small SEN submergence depth, and low casting speed. To maintain a stable double-roll flow pattern, which is often optimal, the argon should be kept safely below a critical level. The chosen optimal nozzle had 45-mm inner bore diameter, downward 15 deg port angle, 2.27 port-to-bore area ratio, and a recessed bottom. The pointed-bottom SEN generates smaller level fluctuations at the meniscus, larger impingement pressure, deeper impingement, and more inclusion entrapment in the strand than the recess-bottom SEN.

Numerical simulation shows that, on occasion, even large bubbles can penetrate deeply and be entrapped through the bottom outlet. This is more likely for 1-mm bubbles than for 5-mm bubbles. Due to the turbulent fluctuations, the motion of the bubbles in the mold is very random and sometimes asymmetrical. Mass balances of inclusions from slag and slab measurements show that around 20 pct of the alumina inclusions are removed from the steel into the mold slag. However, entrainment of the mold slag itself is a critical problem. Inclusions in the steel increase twofold during ladle changes. Slabs cast during the start and end of a sequence have the most inclusions.

REFERENCES

1. H.T. Tsai, W.J. Sammon, and D.E. Hazelton: *Steelmaking Conf. Proc.*, ISS, Warrendale, PA, 1990, vol. 73, pp. 49–59.
2. S. Chakraborty and W. Hill: *77th Steelmaking Conf. Proc.*, ISS, Warrendale, PA, 1994, vol. 77, pp. 389–95.
3. H. Uehara, H. Osanai, J. Hasunuma, K. Hara, T. Nakagawa, M. Yoshida, and S. Yuhara: *La Rev. Metall.-CIT*, 1998, vol. 95 (10), pp. 1273–85.
4. M. Byrne, T.W. Fenicle, and A.W. Cramb: *Steelmaking Conf. Proc.*, 1985, vol. 68, pp. 451–61.

5. M. Byrne, T.W. Fenicle, and A.W. Cramb: *Iron Steelmaker*, 1988, vol. 15 (6), pp. 41–50.
6. M. Byrne, T.W. Fenicle, and A.W. Cramb: *ISS Trans.*, 1989, vol. 10, pp. 51–60.
7. P. Rocabois, J.-N. Pontoire, V. Delville, and I. Marolleau: *ISSTech2003 Conf. Proc.*, ISS, Warrendale, PA, 2003, pp. 995–1006.
8. A. Jungreithmeier, E. Pissenberger, K. Burgstaller, and J. Mortl: *ISSTech2003 Conf. Proc.*, ISS, Warrendale, PA, 2003, pp. 227–40.
9. A.R. Obman, W.T. Germanoski, and R.C. Sussman: *in 64th Steelmaking Conf. Proc*, ISS, Warrendale, PA, 1981, vol. 64, pp. 254–58.
10. J. Yoshida, M. Iguchi, and S. Yokoya: *Tetsu-to-HaganÅ*, 2001, vol. 87 (8), pp. 529–35.
11. N.A. McPherson: *Steelmaking Conf. Proc.*, ISS, Warrendale, PA, 1985, vol. 68, pp. 13–25.
12. H. Jacobi, H.-J. Ehrenberg, and K. Wunnenberg: *Stahl Eisen.*, 1998, vol. 118 (11), pp. 87–94.
13. T. Wei and F. Oeters: *Steel Res.*, 1992, vol. 63 (2), pp. 60–68.
14. M. Iguchi, Y. Sumida, R. Okada, and Z. Morita: *Tetsu-to-HaganÅ*, 1993, vol. 79 (5), pp. 569–75.
15. S.-H. Kim and R.J. Fruehan: *Metall. Trans. B*, 1987, vol. 18B, pp. 381–90.
16. M. Iguchi, Y. Sumida, R. Okada, and Z.-I. Morita: *ISIJ Int.*, 1993, vol. 34 (2), pp. 164–70.
17. R. McDavid and B.G. Thomas: *Metall. Mater. Trans. B*, 1996, vol. 27B, pp. 672–85.
18. B.G. Thomas, X. Huang, and R.C. Sussman: *Metall. Mater. Trans. B*, 1994, vol. 25B, pp. 527–47.
19. T. Teshima, J. Kubota, M. Suzuki, K. Ozawa, T. Masaoka, and S. Miyahara: *Tetsu-to-HaganÅ*, 1993, vol. 79 (5), pp. 576–82.
20. J. Kubota, K. Okimoto, A. Shirayama, and H. Murakami: *Proc. 6th Int. Iron and Steel Congr*, Iron and Steel Institute of Japan, Tokyo, 1990, vol. 3, pp. 356–63.
21. J. Kubota, K. Okimoto, M. Suzuki, A. Shirayama, and T. Masaoka: *ISC. 6th Int. Iron and Steel Congr.*, vol. 3, *Steelmaking I*, Nagoya, Japan, Oct. 21–26, ISIJ, Tokyo, 1990, pp. 356–63.
22. Y. Sasabe, S. Kubota, A. Koyama, and H. Miki: *ISIJ Int.*, 1990, vol. 30 (2), pp. 136–41.
23. J. Kubota, K. Okimoto, A. Shirayama, H. Murakami: in *Mold Operation for Quality and Productivity*, A.W. Cramb E. Szekeres, eds., ISS, Warrendale, PA, 1991.
24. J. Kubota, K. Okimoto, A. Shirayama, and H. Murakami: *Steelmaking Conf. Proc.*, ISS, Warrendale, PA, 1991, vol. 74, pp. 233–41.
25. B.G. Thomas: in *Making, Shaping and Treating of Steel: Continuous Casting*, A. Cramb, ed., AISE Steel Foundation, vol. 5, Pittsburgh, PA, 2003, pp. 14.1–14.41.
26. W.H. Emling, T.A. Waugaman, S.L. Feldbauer, and A.W. Cramb: *77th Steelmaking Conf. Proc.*, ISS, Warrendale, PA, 1994, vol. 77, pp. 371–79.
27. S. Feldbauer and A. Cramb: *PTD Conf. Proc.*, ISS, Warrendale, PA, 1995, vol. 13, pp. 327–40.
28. T. Honeyands and J. Herbertson: *Steel Res.*, 1995, vol. 66 (7), pp. 287–93.
29. M. Gebhard, Q.L. He, and J. Herbertson: *Steelmaking Conf. Proc.*, ISS, Warrendale, PA, 1993, vol. 76, pp. 441–46.
30. W.H. Emling, T.A. Waugaman, S.L. Feldbauer, and A.W. Cramb: *Steelmaking Conf. Proc.*, Chicago, IL, Apr. 13–16, 1997, ISS, Warrendale, PA, 1994, vol. 77, pp. 371–79.
31. K.I. Afanas'Eva and G.P. Iventsov: *Stal*, 1958, vol. 18 (7), pp. 599–604.
32. N.T. Mills and L.F. Barnhardt: *J. Met.*, 1971, vol. 23 (11), pp. 37–43.
33. N.T. Mills and L.F. Barnhardt: *Open Hearth Proc.*, TMS-AIME, Warrendale, PA, 1971, vol. 54, pp. 303–15.
34. J. Szekely and R.T. Yadoya: *Metall. Trans. B*, 1972, vol. 3B, pp. 2673–80.
35. L.J. Heaslip and J. Schade: *Iron Steelmaker*, 1999, vol. 26 (1), pp. 33–41.
36. L.J. Heaslip, I.D. Sommerville, A. McLean, L. Swartz, and W.G. Wilson: *Iron Steelmaker*, 1987, vol. 14 (8), pp. 49–64.
37. D. Gupta, S. Subramaniam, and A.K. Lahiri: *Steel Res.*, 1991, vol. 62 (11), pp. 496–500.
38. D. Gupta, S. Chakraborty, and A.K. Lahiri: *ISIJ Int.*, 1997, vol. 37 (7), pp. 654–58.
39. D. Gupta and A.K. Lahiri: *Metall. Mater. Trans. B*, 1996, vol. 27B, pp. 757–64.
40. D. Gupta and A.K. Lahiri: *Metall. Mater. Trans. B*, 1994, vol. 27B, pp. 695–98.
41. D. Gupta and A.K. Lahiri: *Ironmaking Steelmaking*, 1996, vol. 23 (4), pp. 361–63.
42. H. Tanaka, H. Kuwatori, and R. Nisihara: *Tetsu-to-HaganÅ*, 1992, vol. 78 (5), pp. 761–66.
43. M. Iguchi, J. Yoshida, T. Shimzu, and Y. Mizuno: *ISIJ Int.*, 2000, vol. 40 (7), pp. 685–91.
44. Z. Wang, K. Mukai, and D. Izu: *ISIJ Int.*, 1999, vol. 39 (2), pp. 154–63.
45. M. Iguchi and N. Kasai: *Metall. Mater. Trans. B*, 2000, vol. 31B, pp. 453–60.
46. B.G. Thomas, L.J. Mika, and F.M. Najjar: *Metall. Trans. B*, 1990, vol. 21B, pp. 387–400.
47. X. Huang and B.G. Thomas: *Can. Metall. Q.*, 1998, vol. 37 (304), pp. 197–212.
48. J. Herbertson, Q.L. He, P.J. Flint, and R.B. Mahapatra: *Steelmaking Conf. Proc.*, ISS, Warrendale, PA, 1991, vol. 74, pp. 171–85.
49. J. Herbertson and P. Austin: *Modelling of Casting, Welding, and Advanced Solidification Processes-VI*, T.S. Piwonka, V. Voller, and L. Katgerman, eds., Palm Coast, FL, 1993, TMS, Warrendale, PA, 1993, vol. VI, pp. 689–700.
50. L. Zhang and B.G. Thomas: Report No. CCC200402, University of Illinois at Urbana–Champaign, Urbana, IL, 2004.
51. Q. Yuan, T. Shi, B.G. Thomas, and S.P. Vanka: *Computational Modeling of Materials, Minerals and Metals Processing*, Seattle, WA, Fe. 180-20, 2002, B. Cross and J.W. Evans, eds., TMS, Warrendale, PA, 2002, pp. 491–500.
52. Q. Wu: *Acta Mathematicae Applacatae Sinica*, 1978, vol. 1 (4), pp. 283–99.
53. D.C. Montgomery: *Design and Analysis of Experiments*, Wiley, New York, NY, 1991.
54. K.T. Fang and Y. Wang: *Numer-Theoretic Methods in Statistics*, Chapman and Hall, New York, NY, 1994.
55. Q. Zhang and Y.-W. Leung: *IEEE Trans. Evolutionary Comput.*, 1999, vol. 3 (1), pp. 53–62.
56. Y.-W. Leung and Y. Wang: *IEEE Trans. Evolutionary Comput.*, 2001, vol. 5 (1), pp. 41–53.
57. W.S. Yang, F. Jona, and O.M. Marcus: *J. Vac. Sci. Technol. B*, 1983, vol. 1 (3), pp. 718–22.
58. Y. Bao, J. Zhu, N. Tian, and B. Xu: *J. Univ. Sci. Technol. Beijing (English Edition)*, 1999, vol. 6 (1), pp. 15–19.
59. R. Sanchez-Perez, R.D. Morales, M. Diaz-Cruz, O. Olivares-Xometl, and J. Palafox-Ramos: *ISIJ Int.*, 2003, vol. 43 (5), pp. 637–46.
60. J. Szekely and V. Stanek: *Metall. Trans.*, 1970, vol. 1, pp. 119–26.
61. B.G. Thomas and L. Zhang: *ISIJ Int.*, vol. 41 (10), pp. 1181–93.
62. S.K. Choudhary and D. Mazumdar: *ISIJ Int.*, 1994, vol. 34 (7), pp. 584–92.
63. S.K. Choudhary and D. Mazumdar: *Steel Res.*, 1995, vol. 66 (5), pp. 199–205.
64. J. Szekely and R.T. Yadoya: *Metall. Trans.*, 1973, vol. 4, pp. 1379–88.
65. S. Asai and J. Szekely: *Ironmaking Steelmaking*, 1975, vol. 3 (3), pp. 205–13.
66. B.E. Launder and D.B. Spalding: *Comp. Meth. Appl. Mech. Eng.*, 1974, vol. 13 (3), pp. 269–89.
67. B.G. Thomas and F.M. Najjar: *Appl. Mathemat. Model.*, 1991, vol. 15 (5), pp. 226–43.
68. D.E. Hershey, B.G. Thomas, and F.M. Najjar: *Int. J. Numer. Methods Fluids*, 1993, vol. 17 (1), pp. 23–47.
69. M. Yao, M. Ichimiya, M. Tamiya, K. Suzuki, K. Sugiyama, and R. Mesaki: *Trans. ISIJ*, 1984, vol. 24 (2), pp. s211–15.
70. M. Yao, M. Ichimiya, S. Kiyohara, K. Suzuki, K. Sugiyama, and R. Mesaki: *68th Steelmaking Conf. Proc.*, ISS-AIME, Warrendale, PA, 1985, pp. 27–33.
71. J. Smagorinsky: *Monthly Weather Rev.*, 1963, vol. 91, pp. 99–164.
72. S. Sivaramakrishnan, B.G. Thomas, and S.P. Vanka: in *Materials Processing in the Computer Age*, V. Voller and H. Henein, eds., TMS, Warrendale, PA, 2000, vol. 3, pp. 189–98.
73. Y. Tanizawa, M. Toyoda, K. Takatani, and T. Hamana: *La Rev. Metall.-CIT*, 1993, vol. 90 (8), pp. 993–1000.

74. I. Sawada, Y. Kishida, K. Okazawa, and H. Tanaka: *Tetsu-to-HaganÅ*, 1993, vol. 79 (2), pp. 160–36.
75. I. Sawada, K. Okazawa, E. Takeuchi, K. Shigematsu, and H. Tanaka: *Nippon Steel Technical Report*, 1995, vol. 67, pp. 7–12.
76. Q. Yuan, S. Sivaramakrishnan, S.P. Vanka, and B.G. Thomas: *Metall. Mater. Trans. B*, 2004, vol. 35B, pp. 967–82.
77. Q. Yuan, B.G. Thomas, and S.P. Vanka: *Metall. Mater. Trans. B*, 2004, vol. 35B, pp. 685–702.
78. Q. Yuan, B.G. Thomas, and S.P. Vanka: *Metall. Mater. Trans. B*, 2004, vol. 35B (4), pp. 703–14.
79. L. Zhang, J. Aoki, and B.G. Thomas: in *Materials Science and Technology 2004 (MSandT'04)*, TMS and AIST, Warrendale, PA, 2004, vol. 2, pp. 161–78.
80. H. Bai and B.G. Thomas: *Metall. Mater. Trans. B*, 2001, vol. 32B, pp. 253–67.
81. H. Bai and B.G. Thomas: *Metall. Mater. Trans. B*, 2001, vol. 32B, pp. 269–84.
82. H. Bai and B.G. Thomas: *Metall. Mater. Trans. B*, 2001, vol. 32B, pp. 702–22.
83. A. Imamura, A. Kusano, and N. Moritama: *Tetsu-to-HaganÅ*, 1992, vol. 78 (3), pp. 101–06.
84. N. Bessho, R. Yoda, and H. Yamasaki: *Proc. 6th Int. Iron and Steel Congr.*, ISIJ, Tokyo, 1990, vol. 3, pp. 340–47.
85. B. Grimm, P. Andrzejewski, K. Wagner, and K.-H. Tacke: *Stahl Eisen.*, 1995, vol. 115 (2), pp. 71–78.
86. B.G. Thomas, Q. Yuan, S. Sivaramakrishnan, T. Shi, S.P. Vanka, and M.B. Assar: *ISIJ Int.*, 2001, vol. 41 (10), pp. 1262–72.
87. L. Zhang, S. Yang, X. Wang, K. Cai, J. Li, X. Wan, and B.G. Thomas: *AISTech2004*, ISS, Warrendale, PA, 2004, pp. 879–94.
88. F.G. Wilson, M.J. Heesom, A. Nicholson, and A.W.D. Hills: *Ironmaking Steelmaking*, 1987, vol. 14 (6), pp. 296–309.
89. X. Huang, B.G. Thomas, and F.M. Najjar: *Metall. Trans. B*, 1992, vol. 23B, pp. 339–56.
90. J. Anagnostopoulos and G. Bergeles: *Metall. Mater. Trans. B*, 1999, vol. 30B, pp. 1095–1105.
91. A. Theodorakakos and G. Bergeles: *Metall. Mater. Trans. B*, 1998, vol. 29B (6), pp. 1321–27.
92. G.A. Panaras, A. Theodorakakos, and G. Bergeles: *Metall. Mater. Trans. B*, 1998, vol. 29B, pp. 1117–26.
93. R.H.M.G. Nabben, R.P.J. Duursma, A.A. Kamperman, and J. L. Lagerberg: *Ironmaking Steelmaking*, 1998, vol. 25 (5), pp. 403–06.
94. *FLUENT6.1-Manual*, Fluent Inc., Lebanon, NH, 2003.
95. G. Shi, L. Zhang, Y. Zheng, J. Zhi, W. Wang, J. Zhang, W. Wang, and X. Wang: *Iron Steel*, 2000, vol. 35 (3), pp. 12–15(in Chinese).
96. J. Birat, M. Larrecq, J. Lamant, and J. Petegnief: in *Mold Operation for Quality and Productivity*, A.W. Cramb and E. Szekeres, eds., ISS, Warrendale, PA, 1991, pp. 3–14.
97. M. Hanao, M. Kawamoto, H. Mizukami, and K. Hanazaki: *Steelmaking Conf. Proc*, ISS, Warrendale, PA, 1999, vol. 82, pp. 63–70.
98. P.H. Dauby, M.B. Assar, and G.D. Lawson: *La Rev. Metall.-CIT*, 2001, vol. 98 (4), pp. 353–66.
99. M.B. Assar, P.H. Dauby, and G.D. Lawson: *Steelmaking Conf. Proc.*, ISS, Warrendale, PA, 2000, vol. 83, pp. 397–411.
100. P.H. Dauby and S. Kunstreich: *ISSTech2003*, ISS, Warrendale, PA, 2003, pp. 491–503.
101. L. Zhang and B.G. Thomas: *ISIJ Int.*, 2003, vol. 43 (3), pp. 271–91.
102. M. Burty, C. Pusse, M. Alvarez, and P. Gauje: *2001 Steelmaking Conf. (ISS)*, Baltimore, MD, 2001, M.A. Baker and D.L. Kanagy, eds., 2001, vol. 84, pp. 89–98.
103. M. Burty, M. Larrecq, C. Pusse, and Y. Zbaczyniak: *PTD Conf. Proc.*, ISS, Warrendale, PA, 1995, vol. 13, pp. 287–92; *La Rev. Metall.-CIT*, 1996, Oct., pp. 1249–55.
104. U. Sjostrom, M. Burty, A. Gaggioli, and J. Radot: *81st Steelmaking Conf. Proc.*, Toronto, March 22–25, 1998, ISS, Warrendale, PA, 1998, vol. 81, pp. 63–71.
105. F.M. Najjar, B.G. Thomas, and D.E. Hershey: *Metall. Mater. Trans. B*, 1995, vol. 26B, pp. 749–65.
106. D. Creech: Master's Thesis, University of Illinois at Urbana–Champaign, Champaign, 1998.
107. Z. Wang, K. Mukai, Z. Ma, M. Nishi, H. Tsukamoto, and F. Shi: *ISIJ Int.*, 1999, vol. 39 (8), pp. 795–803.
108. T. Shi and B.G. Thomas: *Effect of Gas Bubble Size on Fluid Flow in Continuous Casting Mold*, Continuous Casting Consortium at the University of Illinois at Urbana–Champaign, Urbana, IL, 2001, .
109. T. Honeyands, J. Lucas, J. Cambers, and J. Herbertson: *Steelmaking Conf. Proc*, ISS, Warrendale, PA, 1992, vol. 75, pp. 451–59.
110. G. Abbel, W. Damen, G. Decendt, and W. Tiekink: *ISIJ Int.*, 1996, vol. 36, pp. S219–22.
111. L. Kiriha, H. Tosawa, and K. Sorimachi: *VCAMP-ISIJ*, 2000, vol. 13, p. 120.
112. L. Zhang and S. Taniguchi: *Int. Mater. Rev.*, 2000, vol. 45 (2), pp. 59–82.
113. J. Wei, Z. Tian, L. Zhang, K. Cai, and Y. Zhou: *Proc. AISTech 2005 Iron and Steel Technology Conf. Expo.*, AIST, Warrendale, PA, 2005, vol. II, pp. 585–92.
114. L. Zhang, B.G. Thomas, K. Cai, L. Zhu, and J. Cui: *ISSTech2003*, ISS, Warrendale, PA, 2003, pp. 141–56.
115. Q. Yuan, B.G. Thomas, and S.P. Vanka: *ISSTech2003 Conf. Proc.*, ISS, Warrendale, PA, 2003, pp. 913–27.
116. I.R. Lee, J. Chai, and K. Shin: *71th Steelmaking Conf. Proc.*, ISS, Warrendale, PA, 1988, vol. 71, pp. 175–80.